

Highly accurate numerical computation of implicitly defined volumes using the Laplace-Beltrami operator

Johannes Kromer[†] and Dieter Bothe[†]

[†]*Mathematical Modeling and Analysis, Technische Universität Darmstadt
Alarich-Weiss-Strasse 10, 64287 Darmstadt, Germany
Email for correspondence: bothe@mma.tu-darmstadt.de*

Abstract

This paper introduces a novel method for the efficient and accurate computation of the volume of a domain whose boundary is given by an orientable hypersurface which is implicitly given as the iso-contour of a sufficiently smooth level-set function. After spatial discretization, local approximation of the hypersurface and application of the GAUSSIAN divergence theorem, the volume integrals are transformed to surface integrals. Application of the surface divergence theorem allows for a further reduction to line integrals which are advantageous for numerical quadrature. We discuss the theoretical foundations and provide details of the numerical algorithm. Finally, we present numerical results for convex and non-convex hypersurfaces embedded in cuboidal domains, showing both high accuracy and third- to fourth-order convergence in space.

1 Introduction

In the context of a two-phase flow problem in some bounded domain $\mathcal{K} \subset \mathbb{R}^d$ with $d \in \{2, 3\}$, the spatial regions \mathcal{K}^\pm occupied by the respective phases, which are separated by an embedded hypersurface $\Sigma \subset \mathcal{K}$, need to be easily identified. One way to achieve this consists in introducing a phase marker f which, say, is 0 for $\boldsymbol{x} \in \mathcal{K}^+$ and 1 for $\boldsymbol{x} \in \mathcal{K}^-$, respectively. A spatial decomposition of the domain into pairwise disjoint cells \mathcal{K}_i allows to assign to each of those a fraction $f_i := |\mathcal{K}_i|^{-1} \int_{\mathcal{K}_i} f d\boldsymbol{x}$ occupied by the first phase. While cells entirely confined in \mathcal{K}^\pm exhibit a marker value of one or zero, respectively, those intersected by the embedded hypersurface admit $0 < f_i < 1$. This representation provides the conceptual foundation of the well-known Volume-of-Fluid (VOF) method introduced by Hirt and Nichols [1981]. To solve an initial value two-phase flow problem, the above mentioned volume fractions f_i need to be computed for a given domain and hypersurface. If accurate initial values are required, this task becomes particularly challenging for curved hypersurfaces, but also for seemingly simple¹ ones like ellipsoids. Thus, the objective of this work is to develop a numerical method for the accurate computation of those volume fractions.

We first provide some relevant notation needed to precisely formulate the problem under consideration and to sketch the approach proposed in this work. The hypersurface $\Sigma \subset \mathcal{K}$ induces a pairwise disjoint decomposition $\mathcal{K} = \Sigma \cap \mathcal{K}^+ \cup \Sigma \cap \mathcal{K}^-$, where we call \mathcal{K}^- and \mathcal{K}^+ the *interior* and *exterior* subdomain, respectively. For the numerical approximation, the embedding domain \mathcal{K} is decomposed into a set of pairwise disjoint cells \mathcal{K}_i , some of which are intersected by Σ , i.e. they contain patches $\Sigma_i := \Sigma \cap \mathcal{K}_i$ of the hypersurface. Note that $\Sigma = \bigcup \Sigma_i$. Any intersected cell again admits a disjoint decomposition into the hypersurface patch Σ_i , as well as an interior (\mathcal{K}_i^-) and exterior (\mathcal{K}_i^+) segment. The allocation property is inherited from the global decomposition of the embedding space, implying that, in a global sense, any $\boldsymbol{x} \in \mathcal{K}_i \setminus \Sigma_i \subset \mathcal{K} \setminus \Sigma$ is either interior or exterior. It is important to note that, locally, $\partial \Sigma_i \neq \emptyset$, even if the hypersurface is globally closed, i.e. $\partial \Sigma = \emptyset$. Figure 1 exemplifies the notation.

Henceforth we are concerned with a single intersected cell \mathcal{K}_i which is why we drop the cell index i for ease of notation. The hypersurface patch $\Sigma \subset \mathcal{K} \subset \mathbb{R}^d$, with $d \in \{2, 3\}$ denoting the spatial dimension, is assumed to be twice continuously differentiable with a simply connected, piecewise smooth boundary $\partial \Sigma \neq \emptyset$. Furthermore, the following assumptions are imposed:

- i. \mathcal{K} is convex with a boundary composed of planar polygons, $\partial \mathcal{K} = \bigcup \mathcal{F}_k$. For technical simplicity, however, let $\mathcal{K} = [0, 1]^d$, implying that the cell faces \mathcal{F}_k are rectangular. This assumption allows for a single parametrization of the boundary curve segment $\partial \Sigma_k = \Sigma \cap \mathcal{F}_k$. For general convex polyhedra the representation potentially requires a cumbersome piecewise definition.

¹Simple in the sense that the description involves only a small set of parameters.

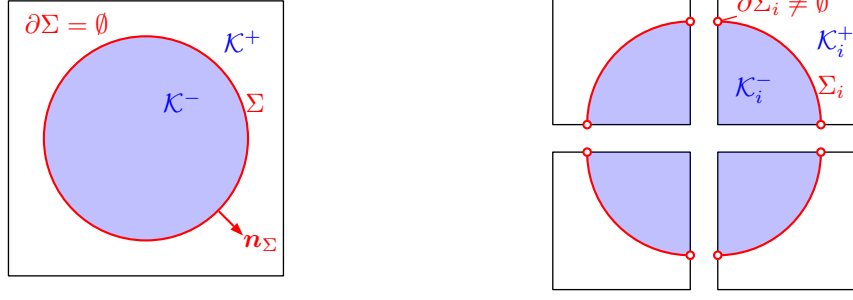


Figure 1: Illustration of the decomposition induced by a closed hypersurface Σ .

- ii. Both the interior and exterior segment contain at least one of the vertices of \mathcal{K} , i.e. the hypersurface boundary $\partial\Sigma$ is not entirely contained in a single face \mathcal{F}_k .
- iii. The division induced by the hypersurface yields simply connected sets \mathcal{K}^\pm and Σ , implying that \mathcal{K} contains a single patch of the hypersurface. This assumption resembles a resolution constraint to the underlying spatial discretization.
- iv. For the principal curvatures κ_i it holds that $\kappa_i d_{\mathcal{K}} \lesssim 10^{-2}$, where $d_{\mathcal{K}}$ is a characteristic length of the cell \mathcal{K} , e.g. the smallest edge length if \mathcal{K} is a cuboid. Note that this assumption actually is a resolution requirement.

Figure 2 illustrates selected admissible and non-admissible setups.

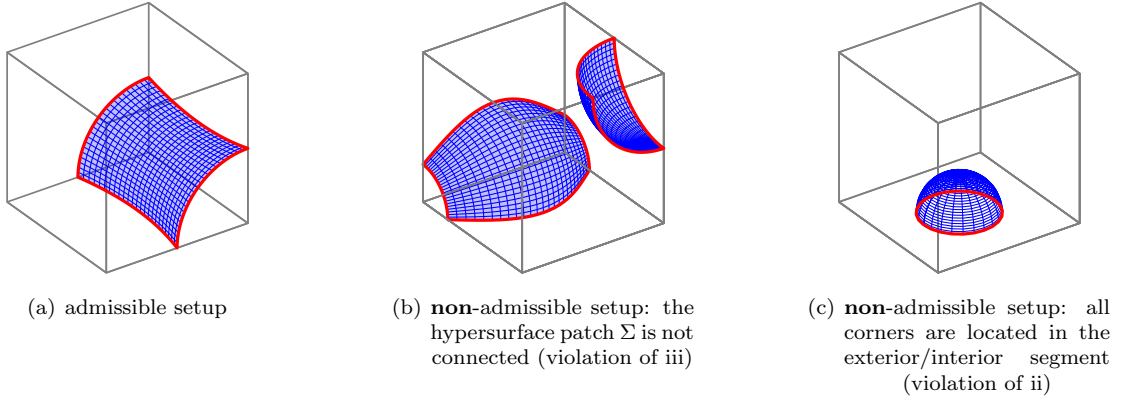


Figure 2: Admissible and non-admissible intersection topologies of interface Σ and cell \mathcal{K} .

We are interested in the evaluation of

$$\text{vol}(\mathcal{K}^-) = \int_{\mathcal{K}^-} 1 \, d\mathbf{x} \quad (1)$$

and employ the GAUSSIAN divergence theorem to get

$$= \frac{1}{3} \int_{\partial\mathcal{K}^-} \langle \mathbf{x}, \mathbf{n} \rangle \, do = \frac{1}{3} \left[\int_{\partial\mathcal{K}^- \setminus \Sigma} \langle \mathbf{x}, \mathbf{n}_{\partial\mathcal{K}^-} \rangle \, do + \int_{\Sigma} \langle \mathbf{x}, \mathbf{n}_{\Sigma} \rangle \, do \right], \quad (2)$$

where $\langle \mathbf{a}, \mathbf{b} \rangle := \mathbf{a}^\top \mathbf{b}$ is the standard inner product for $\mathbf{a}, \mathbf{b} \in \mathbb{R}^d$ and \mathbf{n}_{Σ} denotes the unit normal to Σ , pointing towards the exterior. Note that, by assumption, $\partial\mathcal{K}^- \setminus \Sigma$ is a piecewise planar domain which considerably simplifies the numerical approximation of the associated integral. In contrast, the evaluation of the surface integral features some difficulties, one being the implicit definition of the integration domain itself. The key idea of the presented approach

is the exploitation of the surface divergence theorem associated to Σ . For this purpose, assume for the moment that $u \in H^2(\Sigma)$ is a given solution of LAPLACE-BELTRAMI equation

$$\Delta_{\Sigma} u = \langle \mathbf{x}, \mathbf{n}_{\Sigma} \rangle \quad \text{on } \Sigma, \quad (3)$$

where Δ_{Σ} denotes the LAPLACE-BELTRAMI operator; cf. subsection 2.3. The existence and regularity of the solution u can be proven by application of the according theorems of elliptic partial differential equations. At this point, it is worth noting that the regularity of u crucially depends on the regularity of the underlying hypersurface Σ . However, since we only consider hypersurfaces of class C^{∞} within this work, u exhibits maximal regularity. Then application to the rightmost expression in eq. (2) yields

$$\int_{\Sigma} \langle \mathbf{x}, \mathbf{n}_{\Sigma} \rangle d\sigma = \int_{\partial\Sigma} \langle \nabla_{\Sigma} u, \mathbf{n}_{\partial\Sigma} \rangle dl, \quad (4)$$

where ∇_{Σ} and $\mathbf{n}_{\partial\Sigma}$ denote the surface gradient associated to Σ and the outward-pointing boundary normal, respectively. Note that $\mathbf{n}_{\partial\Sigma}$ is in the tangent space of Σ at \mathbf{x}_0 , i.e. $\mathbf{n}_{\partial\Sigma} \in T_{\Sigma}(\mathbf{x}_0)$. The introduction of appropriate boundary conditions for eq. (3) and properties of the sought solution are deferred to subsection 2.1. An analytical solution to eq. (3) cannot be found for general hypersurfaces Σ . For the numerical solution within this work, we approximate the hypersurface locally and apply two different approaches: (i) a variational formulation of eq. (3), using a PETROV-GALERKIN approach. While the test functions are chosen to be LEGENDRE polynomials, the choice of the ansatz functions has to be in accordance with the structure of the right-hand side, i.e. $\langle \mathbf{x}, \mathbf{n}_{\Sigma} \rangle$. (ii) A comparison of polynomial coefficients. The meaning and motivation for this choice will become clear below.

1.1 Literature review on volume computation

The computation of volumes emerging from the intersection of curved hypersurfaces and polygonally bounded domains (e.g., polyhedra and cuboids) has been addressed in several publications up to this date. Some of the presented approaches exploit the application of appropriate divergence theorems in order to reduce the integral dimension, while others employ direct quadrature.

The approach of Bna et al. [2015] involves direct computation of integrals with discontinuous integrands by means of quadrature, where the boundaries of the integration domain are computed by a root finding algorithm. While their algorithm involves quite some computational effort, it is able to handle non-smooth hypersurfaces. Min and Gibou [2007] develop an algorithm for geometric integration over irregular domains. To obtain the hypersurface position of an intersected polyhedron, the level-set function is evaluated at the corners, allowing for a linear approximation of its respective roots on the edges. Subsequent decomposition of the polyhedron into simplices allows for straightforward evaluation of the desired integrals. Smereka [2006] and the series of papers by Wen [2007, 2009, 2010] are concerned with the numerical evaluation of delta-function integrals in three spatial dimensions. Considering a cuboid intersected by a hypersurface, the concept of Wen is to rewrite the integral over a three-dimensional delta-function as an integral over one of the cell faces, where the integrand is a one-dimensional delta function. All of the above approaches however imply considerable computational effort and complex case-dependent implementations.

Despite covering a different set of applications, namely the computation of integrals over implicitly given hypersurfaces, the work of Müller et al. [2013] is close in spirit to the present paper. The concept underlying their approach is the construction of quadrature nodes and weights from a given level-set function, where the computation of a divergence-free basis of polynomials allows to reduce the spatial problem dimension by one. By recursive application of this concept, integrals over implicitly defined domains and hypersurfaces in \mathbb{R}^3 are transformed to line-integrals. While the method of Müller et al. [2013] is computationally highly efficient and exhibits high accuracy, the numerical tests shown by the authors only cover level-set functions of low polynomial order, i.e. hypersurfaces with few geometric details and exclusively globally convex ones. In section 4, we provide results for both locally and globally non-convex hypersurfaces.

1.2 Overall strategy

The strategy of the presented algorithm consists of two parts. At first, the hypersurface Σ , being defined implicitly as the zero iso-contour of a level-set function $\phi \in C^2(\mathcal{K})$, is locally represented as the graph of a (height) function h_{Σ} over some parameter set $\mathcal{S}_{\Sigma} \subset \mathbb{R}^{d-1}$, i.e.

$$\Sigma = \{ \mathbf{g}_{\Sigma}(\mathbf{t}) : \mathbf{t} \in \mathcal{S}_{\Sigma} \} \quad \text{with} \quad \mathbf{g}_{\Sigma} = [t_i, h_{\Sigma}(\mathbf{t})]^{\top}, \quad (5)$$

and parameters $\mathbf{t} := \{t_i, \dots, t_{d-1}\}$. The coordinate system based in $\mathbf{x}_0 \in \Sigma$ is spanned by the unit normal and the $d - 1$ eigenvectors $\boldsymbol{\tau}_i$ of the associated WEINGARTEN map, i.e. the directions of the principal curvatures. The

associated eigenvalues are the principal curvatures κ_i , corresponding to the reciprocal radii of the osculating circles. A local approximation yields a purely quadratic height function h_Γ . For the remainder of this work, the approximated hypersurface will be denoted by Γ , where quantities and operators introduced for Σ are defined analogously. Subsection 2.2 covers the mathematical details of the approximation. However, in what follows we assume the base point \mathbf{x}_0 , the coordinate system $\{\boldsymbol{\tau}_i, \mathbf{n}_\Sigma\}$ and the principal curvatures κ_i to be given. Exploiting the graph description of the interface allows to transform the integration domain to the associated parameter set \mathcal{S}_Σ , i.e.

$$\int_{\Sigma} \langle \mathbf{x}, \mathbf{n}_\Sigma \rangle d\sigma = \int_{\mathcal{S}_\Sigma} \langle \mathbf{g}_\Sigma(\mathbf{t}), \mathbf{n}_\Sigma(\mathbf{g}_\Sigma(\mathbf{t})) \rangle \mathcal{D}\mathcal{F}(\mathbf{g}_\Sigma) d\mathbf{t}, \quad (6)$$

with $\mathcal{D}\mathcal{F}(\mathbf{g}_\Sigma) := \sqrt{\det(\mathbf{J}_{\mathbf{g}_\Sigma}^T \mathbf{J}_{\mathbf{g}_\Sigma})}$ the functional determinant of \mathbf{g}_Σ , where $\mathbf{J}_{\mathbf{g}_\Sigma}$ denotes the JACOBIAN. To facilitate the numerical treatment, the parameter set is approximated by a polygon which, in general, is neither a super- nor a subset of the true parameter set, cf. figure 6. We will discuss the implications of this property in subsection 2.4. The second part of the strategy is a numerical solution of the surface LAPLACE-BELTRAMI equation. The first concept comprises the application of a PETROV-GALERKIN approach on the variational formulation, i.e. $\Delta_\Gamma u = \langle \mathbf{x}, \mathbf{n}_\Gamma \rangle$ is replaced by

$$\sum_{j=1}^N \hat{u}_j \int_{\Gamma} \varphi_i^t \Delta_\Gamma \varphi_j^a d\sigma = \int_{\Gamma} \langle \mathbf{x}, \mathbf{n}_\Gamma \rangle \varphi_i^t d\sigma \quad \forall \quad 1 \leq i \leq N \quad \text{with} \quad u = \sum_{j=1}^N \hat{u}_j \varphi_j^a, \quad (7)$$

where φ_i^t and φ_j^a are the test and ansatz functions, respectively. The derivation of eq. (7) along with a sketch of the solution strategy are the subject of subsection 2.4. The second concept involves the comparison of coefficients of a polynomial expression, allowing to restrict the deviation of the exact and numerical solution to polynomials of higher order, which become negligible for sufficiently small parameter sets. Subsection 2.5 provides the details.

1.3 Outline

Section 2 introduces the notation and derives mathematical details for two and three spatial dimensions, where basic facts from differential geometry are placed to A. Since the representation of hypersurfaces is of key importance, subsection 2.2 comprises the introduction of local coordinates, as well as an approximation using the WEINGARTEN map. Subsequently, we introduce the LAPLACE-BELTRAMI operator, both in local coordinates and in a comprehensible level-set notation. For certain classes of hypersurfaces, eq. (3) admits analytical solutions, which will be presented and employed to discuss the admissibility of boundary conditions for eq. (3). Finally, this section comprises the numerical solution approaches, namely the comparison of coefficients of polynomials as well as the PETROV-GALERKIN approach, with a focus on the parameter set \mathcal{S}_Γ of the graph representation of Γ . Section 3 introduces the numerical algorithm, where details of the implementation are provided both for the approximation of the hypersurface and the assembly and solution of the linear system of equations resulting from the variational formulation. Moreover, we provide some details of the coefficient comparison. Section 4 is concerned with several numerical experiments for $d = 3$ spatial dimensions and discusses the results. Finally, section 5 concludes the presented work and formulates a further outlook.

2 Mathematical concept of the approach

2.1 Boundary conditions

Note that the application of the divergence theorem, cf. eq. (4), does not require any boundary conditions for the sought function u . In order to facilitate numerical treatment by exploitation of divergence theorems, it is favorable to either prescribe DIRICHLET or NEUMANN boundary conditions. While in theory, the problem at hand does admit solutions² fulfilling DIRICHLET conditions, say, e.g., $u|_{\partial\Sigma} = 0$, the desired application of the surface divergence theorem, cf. eq. (4), obviously prohibits homogeneous NEUMANN boundary conditions, because $\int_{\partial\Sigma} \langle \nabla_\Sigma u, \mathbf{n}_{\partial\Sigma} \rangle dl = 0$ for $\nabla_\Sigma u|_{\partial\Sigma} = \mathbf{0}$. In the context of the numerical algorithm presented here, however, we are only interested in the approximation of *any* regular solution u , whose surface gradient is evaluated on $\partial\Sigma$. With an appropriate ansatz space ensuring regularity, both the variational formulation and the comparison of coefficients provide a unique solution. Hence, the presented approach does not require to specify particular boundary conditions. The admissibility of DIRICHLET boundary conditions is deferred to the last paragraph in subsection 2.3.

²For further mathematical details on the existence of solutions, the reader is referred to Prüss and Simonett [2016] and the references given therein.

2.2 Approximation of hypersurfaces in local coordinates

As shown in the appendix, cf. eq. (49), under the general assumptions formulated above, the hypersurface patch Γ can be parametrized as the graph of a height function, i.e.³

$$\Sigma = \{\mathbf{x}_0 + t_i \boldsymbol{\tau}_i + h_\Sigma(\mathbf{t}) \mathbf{n}_0 : \mathbf{t} \in \mathcal{S}_\Sigma\} \quad \text{with} \quad h_\Sigma \in \mathcal{C}^2(\mathcal{S}_\Sigma) \quad \text{and} \quad \mathbf{n}_0 := \mathbf{n}_\Sigma(\mathbf{x}_0), \quad (8)$$

where $\{\boldsymbol{\tau}_i, \mathbf{n}_0\}$ forms an orthonormal system for fixed \mathbf{x}_0 . Also, an appropriate shift of coordinates ensures $\mathbf{x}_0 = \mathbf{0}$. The computation of the height function $h_\Sigma = h_\Sigma(\mathbf{t}; \mathbf{x}_0)$ requires to solve the nonlinear implicit equation $\phi_\Sigma(\mathbf{x}_0 + t_i \boldsymbol{\tau}_i + h_\Sigma \mathbf{n}_0) = 0$. Since this may be cumbersome, we choose to approximate the hypersurface around \mathbf{x}_0 by the graph of an approximated height function, based on the principal curvatures provided by the WEINGARTEN map. We obtain

$$\Gamma = \{\mathbf{g}_\Gamma(\mathbf{t}) : \mathbf{t} \in \mathcal{S}_\Gamma\} \quad \text{with} \quad \mathbf{g}_\Gamma(\mathbf{t}) := \mathbf{x}_0 + t_i \boldsymbol{\tau}_i + h_\Gamma \mathbf{n}_0, \quad (9)$$

where the height function reads

$$h_\Gamma = \frac{1}{2} \sum_{i=1}^{d-1} \kappa_i t_i^2, \quad \text{with} \quad \|h_\Sigma - h_\Gamma\| = \mathcal{O}(\|\mathbf{t}\|^4). \quad (10)$$

Note that in general, as mentioned above, the respective parameter sets do *not* coincide, i.e. $\mathcal{S}_\Sigma \neq \mathcal{S}_\Gamma$. However, the parameter set deviation $\Delta\mathcal{S}_\Sigma := (\mathcal{S}_\Sigma \setminus \mathcal{S}_\Gamma) \cup (\mathcal{S}_\Gamma \setminus \mathcal{S}_\Sigma)$ will be small if the characteristic length $d_\mathcal{K}$ of cell \mathcal{K} suffices $d_\mathcal{K} \kappa_i \leq 10^{-2}$, see figure 3 for an illustration.

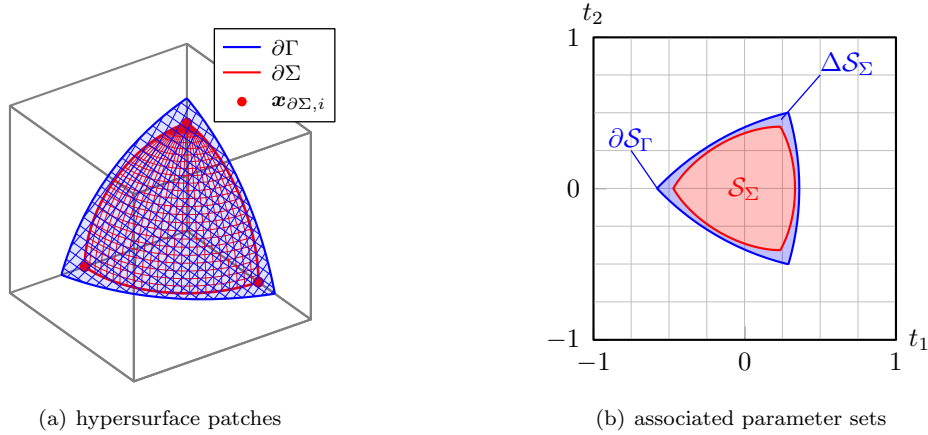


Figure 3: Deviation of parameter sets induced by approximation (light blue) of the hypersurface $\Sigma = \partial\mathcal{B}_R(\mathbf{0}) \cap \mathcal{K}$ (red mesh) around $\mathbf{x}_0 = \frac{1}{3}[1, 1, 1]$ with $\kappa_i = \frac{1}{R}$ and $\mathbf{n}_0 = \frac{-1}{\sqrt{3}}[1, 1, 1]$. In general, it holds that $\mathcal{S}_\Gamma \not\supset \mathcal{S}_\Sigma$, i.e. the parameter set of the approximation does not contain the true parameter set.

Furthermore, the graph representation of Σ , cf. eq. (9), allows to assign to any $f : \Sigma \mapsto \mathbb{R}$ a function $f^\Sigma : \mathcal{S}_\Sigma \mapsto \mathbb{R}$ with $f^\Sigma := f \circ \mathbf{g}_\Sigma$.

2.3 Representations of the Laplace-Beltrami operator

On a curved manifold Σ the correspondent to the LAPLACE operator $\Delta u = \partial_{ii} u$ in EUCLIDEAN space, being defined as the divergence of the gradient of a scalar function is the LAPLACE-BELTRAMI operator (associated to Σ), defined as $\Delta_\Sigma u := \text{div}_\Sigma \nabla_\Sigma u$. In what follows, we derive the concrete form of the LAPLACE-BELTRAMI operator for implicitly (in terms of a level-set) and explicitly (as the graph of a function) defined hypersurfaces. For the level-set case, the authors could not find the specific representations in the literature. Furthermore, we present specific analytical solutions of the LAPLACE-BELTRAMI equation emerging from the computation of volumes, cf. eq. (3). In the sequel, Γ represents a member of the class of hypersurfaces given by eq. (9).

³To ease notation and avoid explicit notations for different values of d , henceforth the EINSTEIN summation convention applies.

Level-set representation For a hypersurface $\Sigma \subset \mathbb{R}^d$ defined by the iso-contour of a smooth level-set $\phi \in \mathcal{C}^2(\mathbb{R}^d)$, one obtains

$$\Delta_\Sigma u = \mathbf{P}_\Sigma : \nabla^2 u - \frac{\langle \nabla u, \nabla \phi \rangle}{\langle \nabla \phi, \nabla \phi \rangle} \left(\mathbf{P}_\Sigma : \nabla^2 \phi \right) = \mathbf{P}_\Sigma : \nabla^2 u - \langle \nabla u, \mathbf{n}_\Sigma \rangle \frac{\mathbf{P}_\Sigma : \nabla^2 \phi}{\langle \nabla \phi, \nabla \phi \rangle^{\frac{1}{2}}}, \quad (11)$$

where $\mathbf{P}_\Sigma := \mathbf{I} - \mathbf{n}_\Sigma \otimes \mathbf{n}_\Sigma$, $\nabla^2 f := \partial_{ij} f \mathbf{e}_i \otimes \mathbf{e}_j$ and $\mathbf{A} : \mathbf{B} := \text{tr}(\mathbf{A}^\top \mathbf{B})$ denote the tangential projection, HESSIAN matrix and real tensor contraction, respectively. Here, we would like to emphasize the relation to the mean curvature

$$\kappa_\Sigma := \text{div}_\Sigma(-\mathbf{n}_\Sigma) = \sum_{i=1}^{d-1} \kappa_i = -\frac{\mathbf{P}_\Sigma : \nabla^2 \phi}{\langle \nabla \phi, \nabla \phi \rangle^{\frac{1}{2}}}. \quad (12)$$

Graph representation (d = 2) If the hypersurface is given as the graph of a function $h_\Sigma(\mathbf{t}) : \mathcal{S}_\Sigma \mapsto \mathbb{R}$ with parameter set $\mathcal{S}_\Sigma \subset \mathbb{R}$, introducing $\partial_i := \frac{\partial}{\partial t_i}$ and $\partial_{ij} := \frac{\partial^2}{\partial t_i \partial t_j}$, one obtains

$$\Delta_\Sigma u = \partial_{11} u \frac{1}{1 + (\partial_1 h_\Sigma)^2} - \partial_1 u \frac{\partial_{11} h_\Sigma \partial_1 h_\Sigma}{\left(1 + (\partial_1 h_\Sigma)^2\right)^2}. \quad (13)$$

The above form is easily derived from eq. (11) with $\phi(\mathbf{t}) = t_2 - h_\Sigma(t_1)$ and $u(\mathbf{t}) = u(t_1)$. For height functions of purely quadratic form, i.e. $h_\Gamma = \frac{\kappa_1^2 t_1^2}{2}$, cf. eq. (9), eq. (13) becomes

$$\Delta_\Gamma u = \partial_{11} u \frac{1}{1 + \kappa_1^2 t_1^2} - \partial_1 u \frac{\kappa_1^2 t_1}{\left(1 + \kappa_1^2 t_1^2\right)^2}. \quad (14)$$

The right-hand sides become

$$\langle \mathbf{x}, \mathbf{n}_\Sigma \rangle = \frac{-h_\Sigma}{\sqrt{1 + (\partial_1 h_\Sigma)^2}} \quad \text{and} \quad \langle \mathbf{x}, \mathbf{n}_\Gamma \rangle = \frac{-\kappa_1 t_1^2}{2\sqrt{1 + \kappa_1^2 t_1^2}}. \quad (15)$$

Graph representation (d = 3) By arguments analogous to those given above, for the case of three spatial dimensions we have $\phi(\mathbf{t}) = t_3 - h_\Sigma(t_1, t_2)$, yielding

$$\begin{aligned} \Delta_\Sigma u &= \partial_{11} u \frac{1 + \partial_2 h_\Sigma^2}{1 + \partial_1 h_\Sigma^2 + \partial_2 h_\Sigma^2} + \partial_{22} u \frac{1 + \partial_1 h_\Sigma^2}{1 + \partial_1 h_\Sigma^2 + \partial_2 h_\Sigma^2} - \partial_{12} u \frac{2\partial_1 h_\Sigma \partial_2 h_\Sigma}{1 + \partial_1 h_\Sigma^2 + \partial_2 h_\Sigma^2} \\ &\quad - \frac{\partial_1 u \partial_1 h_\Sigma + \partial_2 u \partial_2 h_\Sigma}{\left(1 + \partial_1 h_\Sigma^2 + \partial_2 h_\Sigma^2\right)^2} \left(\partial_{11} h_\Sigma \left(1 + \partial_2 h_\Sigma^2\right) + \partial_{22} h_\Sigma \left(1 + \partial_1 h_\Sigma^2\right) - 2\partial_{12} h_\Sigma \partial_1 h_\Sigma \partial_2 h_\Sigma \right), \end{aligned} \quad (16)$$

which in the purely quadratic case, i.e. with $h_\Gamma = \frac{\kappa_1 t_1^2 + \kappa_2 t_2^2}{2}$, simplifies to

$$\begin{aligned} \Delta_\Gamma u &= \partial_{11} u \frac{1 + \kappa_2^2 t_2^2}{1 + \kappa_1^2 t_1^2 + \kappa_2^2 t_2^2} + \partial_{22} u \frac{1 + \kappa_1^2 t_1^2}{1 + \kappa_1^2 t_1^2 + \kappa_2^2 t_2^2} - \partial_{12} u \frac{2\kappa_1 \kappa_2 t_1 t_2}{1 + \kappa_1^2 t_1^2 + \kappa_2^2 t_2^2} \\ &\quad - \frac{\partial_1 u \kappa_1 t_1 + \partial_2 u \kappa_2 t_2}{\left(1 + \kappa_1^2 t_1^2 + \kappa_2^2 t_2^2\right)^2} \left(\kappa_1 \left(1 + \kappa_2 t_2^2\right) + \kappa_2 \left(1 + \kappa_1 t_1^2\right) \right). \end{aligned} \quad (17)$$

Note that the application of the operator given in eq. (17) to a function preserves the following symmetry:

$$\begin{aligned} u(t_1, t_2) = u(t_1, -t_2) &\implies [\Delta_\Sigma u(\mathbf{t})]_{|\mathbf{t}=[x_1, x_2]} = [\Delta_\Sigma u(\mathbf{t})]_{|\mathbf{t}=[x_1, -x_2]} \\ u(t_1, t_2) = u(-t_1, t_2) &\implies [\Delta_\Sigma u(\mathbf{t})]_{|\mathbf{t}=[x_1, x_2]} = [\Delta_\Sigma u(\mathbf{t})]_{|\mathbf{t}=[-x_1, x_2]} \end{aligned} \quad (18)$$

Analogously to the case above, the right-hand sides become

$$\langle \mathbf{x}, \mathbf{n}_\Sigma \rangle = \frac{-h_\Sigma}{\sqrt{1 + (\partial_1 h_\Sigma)^2 + (\partial_2 h_\Sigma)^2}} \quad \text{and} \quad \langle \mathbf{x}, \mathbf{n}_\Gamma \rangle = \frac{-\kappa_1 t_1^2 - \kappa_2 t_2^2}{2\sqrt{1 + \kappa_1^2 t_1^2 + \kappa_2^2 t_2^2}}. \quad (19)$$

Analytical solutions for $\Delta_\Gamma u = \langle \mathbf{x}, \mathbf{n}_\Gamma \rangle$ For non-planar hypersurfaces Γ in two spatial dimensions with arbitrary but constant $\kappa \in \mathbb{R}$, combining eq. (14) and eq. (15), we obtain the family of solutions

$$u(t_1; \kappa) = u_0 + \left(\frac{1}{18\kappa^3} - \frac{1 + \kappa^2 t_1^2}{30\kappa^3} \right) \left(1 + \kappa^2 t_1^2 \right)^{\frac{3}{2}}, \quad (20)$$

where choosing $u_0 = -\frac{1}{45\kappa^3}$ ensures $u(0; \kappa) = 0$. For planar hypersurfaces, the solution becomes trivial, since $\lim_{\kappa \rightarrow 0} u(t_1; \kappa) = 0$. The existence of an analytical solution implies that the computation of the volume (i.e. the area, since we consider $d = 2$ here) only requires to compute the two intersections, denoted t_1^\pm , of the approximated hypersurface Γ with the cell boundary $\partial\mathcal{K}$, e.g. by a simple NEWTON algorithm. The t_1^\pm are plugged then into eq. (20) to obtain the surface gradient $\nabla_\Sigma u|_{t_1=t_1^\pm}$, which is then used to evaluate the inner product with the boundary normal $\mathbf{n}_{\partial\Sigma}$. Figure 4 illustrates the relevant quantities. Also, an advantage of our approach becomes evident in figure 4(a): for $d = 2$, the approximated hypersurface is not required to be the graph of a function whose independent variable varies along one of the cell edges.

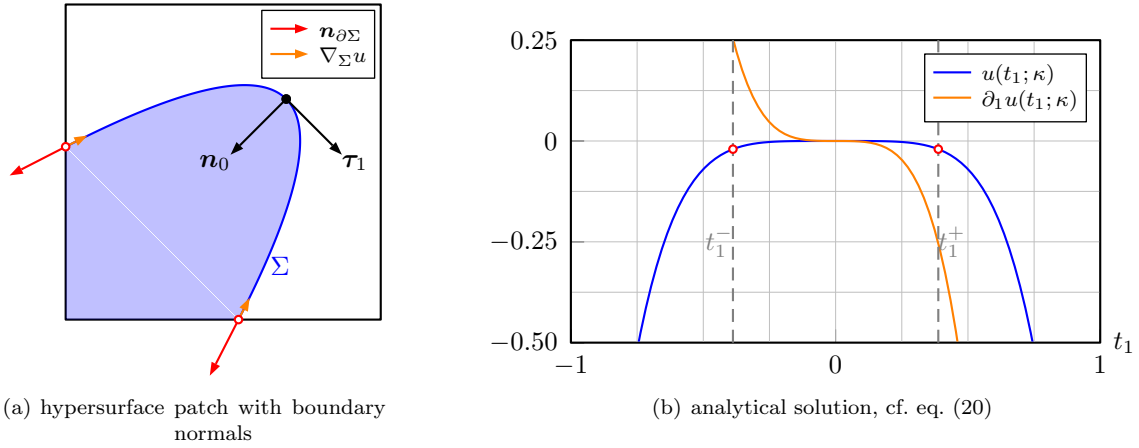


Figure 4: $\kappa = 8$, $\mathbf{n}_0 = \frac{1}{\sqrt{2}}[-1, -1]^\top$, $\mathbf{x}_0 = \frac{7}{10}[1, 1]^\top$

In three spatial dimensions, cf. eq. (17) and eq. (19), a family of analytical solutions can be given for coinciding and constant principal curvatures $\kappa_1 = \kappa_2 = \kappa$, yielding

$$u(\mathbf{t}; \kappa) = u_0 + \left(\frac{1}{24\kappa^3} - \frac{1 + \kappa^2 t_1^2 + \kappa^2 t_2^2}{40\kappa^3} \right) \left(1 + \kappa^2 t_1^2 + \kappa^2 t_2^2 \right)^{\frac{3}{2}}. \quad (21)$$

By choosing $u_0 = -\frac{1}{60\kappa^3}$, one obtains $u(\mathbf{0}; \kappa) = 0$. For the non-trivial case $\kappa \neq 0$, the iso-contours of the analytical solution, i.e. $\mathcal{I}(u; \alpha) := \{\mathbf{t} \in \mathbb{R}^2 : u(\mathbf{t}; \kappa) = \alpha\}$, are circles. This implies that for $\alpha \neq 0$ on a polygonal parameter set \mathcal{S}_Γ , which is preferable for numerical implementation, the function $u|_{\partial\mathcal{S}_\Gamma}$ cannot be constant, especially $u|_{\partial\mathcal{S}_\Gamma} \neq 0$; cf. figure 5. This imposes crucial restrictions on the numerical algorithm for the solution of the variational problem, if, e.g., one seeks to exploit partial integration; cf. eq. (56).

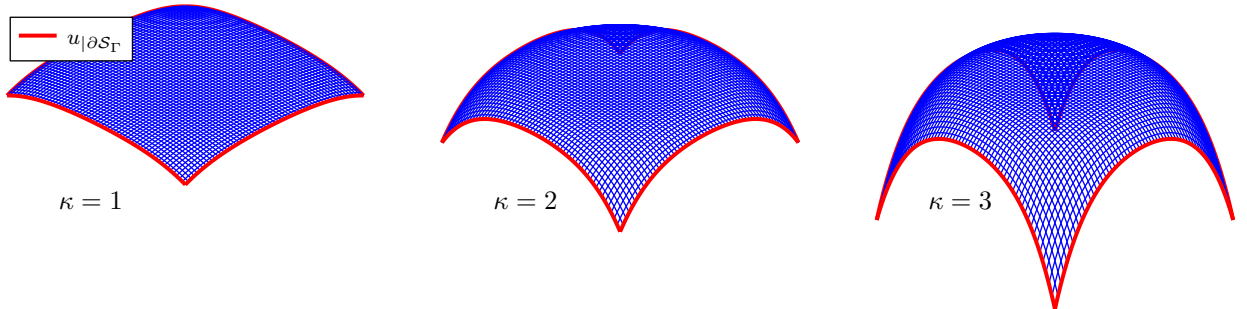


Figure 5: Visualization of eq. (21) for $\mathcal{S}_\Gamma = [-1, 1]^2$ and various κ .

For the general case $\kappa_1 \neq \kappa_2$, an analytical solution could not be found by the authors. Hence, we transform the problem into its variational formulation, in order to make it accessible for numerical treatment.

2.4 Variational formulation and Petrov-Galerkin ansatz

The present subsection is devoted to the variational formulation of $\Delta_\Gamma u = \langle \mathbf{x}, \mathbf{n}_\Gamma \rangle$ for hypersurfaces $\Gamma \subset \mathbb{R}^3$ defined by eq. (9), following a standard approach: we multiply by a test function $\varphi_i^t \in \mathcal{F}_N^t$, approximate the sought solution u by a series of N ansatz functions $\varphi_j^a \in \mathcal{F}_N^a$ and numerically integrate over Γ . Note that because the properties of the analytical solution given in eq. (21), which is desired to be an element of the ansatz function space, prohibit application of DIRICHLET boundary conditions on polygonally bounded parameter sets, and NEUMANN boundary conditions are incompatible within our approach, we do not apply partial integration. The details of the function spaces are provided below. As stated in subsection 2.2, due to the explicit parametrization, any function f mapping from the hypersurface Γ may be expressed as $f^\Gamma = f \circ \mathbf{g}_\Gamma$, with $f^\Gamma : \mathcal{S}_\Gamma \mapsto \mathbb{R}$. Exploiting the integral transformation from eq. (6), one obtains

$$\sum_{j=1}^N \hat{u}_j \int_{\mathcal{S}_\Gamma} \varphi_i^t(\mathbf{t}) \Delta_\Gamma \varphi_j^a(\mathbf{t}) \mathcal{D}\mathcal{F}(\mathbf{g}_\Gamma(\mathbf{t})) d\mathbf{t} = \int_{\mathcal{S}_\Gamma} f^\Gamma(\mathbf{t}) \varphi_i^t(\mathbf{t}) \mathcal{D}\mathcal{F}(\mathbf{g}_\Gamma(\mathbf{t})) d\mathbf{t} \quad \text{or} \quad \mathbf{A}_\Gamma \hat{\mathbf{u}} = \mathbf{b}_\Gamma, \quad (22)$$

with the functional determinant $\mathcal{D}\mathcal{F}(\mathbf{g}_\Gamma) := \langle \nabla \phi_\Gamma, \nabla \phi_\Gamma \rangle^{\frac{1}{2}} = \sqrt{1 + \kappa_1^2 t_1^2 + \kappa_2^2 t_2^2}$ corresponding to the area of an infinitesimal hypersurface element; cf. subsection 2.3.

Approximation of the parameter set: A direct numerical quadrature of eq. (22) is difficult due to the potentially non-polygonal shape of the parameter set \mathcal{S}_Γ . Therefore we approximate the parameter set by a polygon spanned by the projection of the intersections of the hypersurface with the cell edges; cf. figure 6(b).

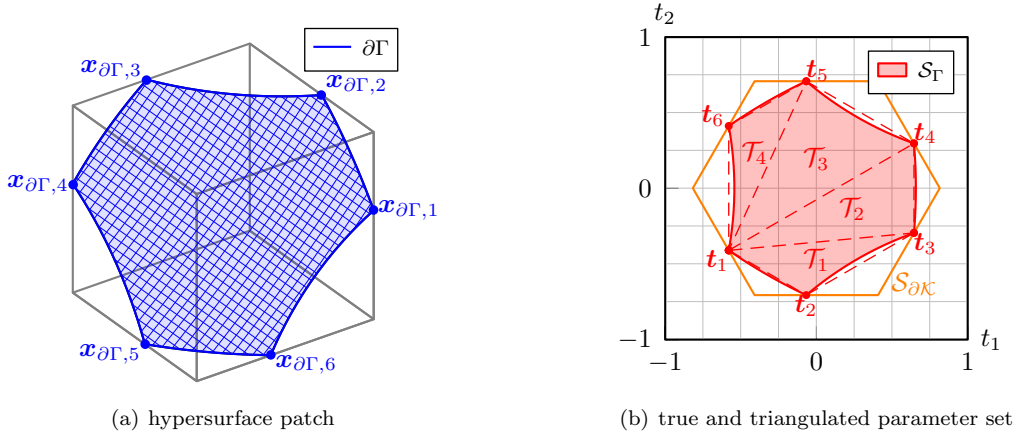


Figure 6: Hypersurface ($\mathbf{x}_0 = \frac{6}{10}[1, 1, 1]$, $\kappa_i = -\frac{1}{2}$ and $\mathbf{n}_0 = \frac{-1}{\sqrt{3}}[1, 1, 1]$) with true (shaded) and triangulated (dashed lines) parameter set, where $\mathcal{S}_{\partial\mathcal{K}}$ is the projection of the cell boundary. Note that the polygon spanned by the projections of the edge intersections (\bullet) does not contain the true parameter set, nor vice versa, i.e. $\bigcup_k \mathcal{T}_k \not\supset \mathcal{S}_\Gamma$ and $\bigcup_k \mathcal{T}_k \not\subset \mathcal{S}_\Gamma$, in general.

The integration over the approximated parameter set $\mathcal{S}_\Gamma \approx \bigcup_k \mathcal{T}_k$ can then be performed by transformation of the respective triangles to the referential square $\mathcal{S}_0 := [0, 1]^2$ (via the referential triangle \mathcal{T}_0) and standard GAUSS-LEGENDRE quadrature, i.e.

$$\int_{\mathcal{T}_k} f(\mathbf{t}) d\mathbf{t} = \int_{\mathcal{T}_0} f(\mathbf{T}_k(\mathbf{u})) \|\det \mathbf{J}_{\mathbf{T}_k}\| d\mathbf{u} = \int_{\mathcal{S}_0} f(\mathbf{T}_k(\mathbf{T}_\mathcal{S}(\mathbf{u}))) u_1 \|\det \mathbf{J}_{\mathbf{T}_k}\| d\mathbf{u} \approx \sum_i f(\hat{\mathbf{t}}_{k,i}) \omega_{k,i}^\Gamma, \quad (23)$$

where $\hat{\mathbf{t}}_{i,k} \in \mathcal{T}_k$ are the quadrature nodes with associated weights $\omega_{k,i}^\Gamma$; cf. figure 7 for an illustration.

Although it would be more convenient to approximate the parameter set by the projection of the cell boundary $\mathcal{S}_{\partial\mathcal{K}}$, say, our numerical experiments have shown that the quality of the parameter set approximation is crucial for the overall accuracy of the algorithm. The accuracy especially suffers from a coarse parameter set approximation for $\kappa_1 \neq \kappa_2$, rapidly decreasing for increasing $|\kappa_1 - \kappa_2|$.

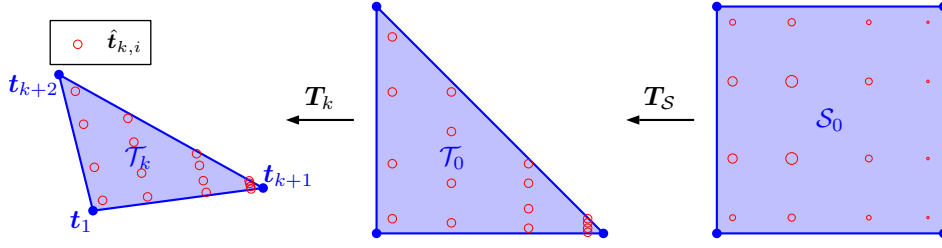


Figure 7: Transformation of triangular integration domain $\mathcal{T}_k \subset \mathbb{R}^2$ to \mathcal{S}_0 . In the reference square, the circle sizes indicate the relative magnitude of the weights $\omega_{k,i}^\Gamma$.

The choice of ansatz and test functions: In order for eq. (22) to be a well-posed problem for $\hat{\mathbf{u}}$, the regularity required for the test functions is $\varphi_i^t \in \mathcal{F}_N^t \subset L^2(\mathcal{S}_\Gamma)$ and for the ansatz functions $\varphi_j^a \in \mathcal{F}_N^a \subset H^2(\mathcal{S}_\Gamma)$, respectively. Since the test functions need not contain any information on the underlying hypersurface, let $\mathcal{F}_N^t = \mathcal{L}_N(t_1) \times \mathcal{L}_N(t_2)$, where $\mathcal{L}_N(x) := \{P_k(x) : 0 \leq k \leq N\}$ is the set of LEGENDRE polynomials up to order N . Preliminary numerical experiments indicated that the ansatz functions φ_i^a have to be chosen in accordance with both the underlying hypersurface Γ and the right-hand side. Here, the ansatz functions contain the norm of an infinitesimal surface element, i.e.

$$\varphi_i^a := \varphi_i^t \langle \nabla \phi_\Gamma, \nabla \phi_\Gamma \rangle^{\frac{3}{2}} = \varphi_i^t \left(1 + \kappa_1^2 t_1^2 + \kappa_2^2 t_2^2 \right)^{\frac{3}{2}}. \quad (24)$$

This choice also ensures that the analytical solution for the volume computation case ($f = \langle \mathbf{x}, \mathbf{n}_\Gamma \rangle$) given in eq. (21) is an element of $\text{span}(\mathcal{F}_N^a)$, which is not possible by choosing polynomial ansatz functions. Also, we would like to emphasize that the above mentioned symmetry properties of the LAPLACE-BELTRAMI operator, cf. eq. (18), for purely quadratic hypersurfaces allows to remove those LEGENDRE polynomials with odd order, since their contributions cancel during the integration.

2.5 Equating polynomial coefficients

Within this subsection, let $g := 1 + \kappa_1^2 t_1^2 + \kappa_2^2 t_2^2$ for ease of notation and assume that $u : \mathbb{R}^2 \mapsto \mathbb{R}$ is polynomial. Note that for the gradient and HESSIAN matrix, respectively, one obtains

$$\begin{aligned} \partial_i \left(u \sqrt{g^3} \right) &= \frac{1}{\sqrt{g}} \left[g^2 \partial_i f + \frac{3}{2} f g \partial_i g \right], \\ \partial_{ij} \left(u \sqrt{g^3} \right) &= \frac{1}{\sqrt{g}} \left[g^2 \partial_{ij} u + \frac{3g}{2} (\partial_i g \partial_j f + \partial_j g \partial_i f + u \partial_{ij} g) + \frac{3f}{2} \partial_i g \partial_j g \right], \end{aligned} \quad (25)$$

where the expressions in parentheses are also polynomial. Inserting the above into the definition of the surface LAPLACE-BELTRAMI operator, cf. eq. (17), and comparing the result with the right-hand side, cf. eq. (19), it becomes evident that the left-hand side of

$$\sqrt{g} \left(\Delta_\Gamma \left(u \sqrt{g^3} \right) - \langle \mathbf{x}, \mathbf{n}_\Gamma \rangle \right) = 0 \quad (26)$$

is a polynomial expression. In fact, one obtains

$$\begin{aligned} \sqrt{g} \Delta_\Gamma \left(t_1^m t_2^n \sqrt{g^3} \right) &= (\kappa_1^2 (m^2 + 4m + 3) + (n^2 + 4n + 3) \kappa_2^2 - \kappa_1 \kappa_2 (2mn + m + n)) t_1^m t_2^n \\ &\quad + (\kappa_1^2 \kappa_2^2 (m^2 + 4m + 3) - \kappa_1 \kappa_2^3 (2mn + 6m + n + 3)) t_1^m t_2^{n+2} \\ &\quad + (\kappa_1^2 \kappa_2^2 (n^2 + 4n + 3) - \kappa_1^3 \kappa_2 (2mn + 6n + m + 3)) t_1^{m+2} t_2^n \\ &\quad + 2\kappa_2^2 (m^2 - m) t_1^{m-2} t_2^{n+2} + (n^2 - n) t_1^m t_2^{n-2} + (m^2 - m) t_1^{m-2} t_2^n \\ &\quad + \kappa_2^4 (m^2 - m) t_1^{m-2} t_2^{n+4} + 2\kappa_1^2 (n^2 - n) t_1^{m+2} t_2^{n-2} \\ &\quad + \kappa_1^4 (n^2 - n) t_1^{m+4} t_2^{n-2}. \end{aligned} \quad (27)$$

Furthermore, the symmetry of $\langle \mathbf{x}, \mathbf{n}_\Gamma \rangle$ implies that any solution u of eq. (26) can only contain even powers of t_i , hence we choose the ansatz

$$u = \sum_{i=0}^N \sum_{j=0}^M \hat{u}_{ij} t_1^{2i} t_2^{2j}, \quad (28)$$

where the $(N + 1)(M + 1)$ coefficients $\hat{\mathbf{u}} := \{\hat{u}_{ij}\}$ are obtained from comparison of polynomial coefficients. As can be seen from eq. (27), the modified LAPLACE-BELTRAMI operator $\tilde{\Delta}_\Gamma u := \sqrt{g} \Delta_\Gamma (u \sqrt{g^3})$ expands the polynomial span of its argument, implying that the system of equations governing the coefficients \hat{u}_{ij} will be overdetermined for general $\kappa_1 \neq \kappa_2$, since

$$\sum_{i=0}^N \sum_{j=0}^M \hat{u}_{ij} \tilde{\Delta}_\Gamma (t_1^{2i} t_2^{2j}) - \sqrt{g}(\mathbf{x}, \mathbf{n}_\Gamma) = \sum_{i=0}^{N+2} \sum_{j=0}^{M+2} \beta_{ij}(\hat{\mathbf{u}}; \kappa_1, \kappa_2) t_1^{2i} t_2^{2j}. \quad (29)$$

Solving eq. (26) exactly is equivalent to finding $\hat{\mathbf{u}}$ such that $\beta(\hat{\mathbf{u}}; \kappa_1, \kappa_2) = \mathbf{0}$. Since β is linear in $\hat{\mathbf{u}}$, we may write

$$\mathbf{B}_\Gamma \hat{\mathbf{u}} = \mathbf{q}_\Gamma \quad \text{with} \quad \mathbf{B}_\Gamma \in \mathbb{R}^{K \times (N+1)(M+1)} \quad \text{and} \quad \mathbf{q}_\Gamma \in \mathbb{R}^K, \quad (30)$$

where the number of rows K is a function of maximum polynomial orders N, M with $K \geq (N + 1)(M + 1)$. Numerical experiments for $1 \leq N, M \leq 6$ indicate that (i) the matrix \mathbf{B}_Γ does not have full rank, i.e. $\text{rank}(\mathbf{B}_\Gamma) < K$, and (ii) the rank of \mathbf{B}_Γ is $(N + 1)(M + 1)$, cf. table 1. Assume that the elements in β (corresponding to the rows in \mathbf{B}_Γ) are sorted in ascending order with respect to the corresponding powers of \mathbf{t} . Looping over all K rows in \mathbf{B}_Γ , the m -th row is discarded if it is linear dependent on the $m - 1$ previous rows. The polynomials whose coefficients cannot be eliminated are of higher order, i.e. $\mathcal{O}(\|\mathbf{t}\|^{2N+2})$. In the limiting case $\kappa_1 = \kappa_2$, this approach produces the analytical solution given in eq. (21). We would like to emphasize that due to $\text{rank}(\mathbf{B}_\Gamma) = (N + 1)(M + 1)$, the reduced form of eq. (30) can be solved exactly. \mathbf{B} contains the full expansion of the first three entries of the coefficient vector.

Table 1: Number of coefficients K over various $N = M$, with the apparent relation $K - (N + 1)^2 = 4N + 2$.

N	1	2	3	4	5	6
K	10	19	30	43	58	75
$K - (N + 1)^2$	6	10	14	18	22	26

3 The numerical algorithm

Figure 8 contains a schematic flowchart⁴ of the developed numerical algorithm. The intersections $\mathbf{x}_{\partial\Sigma, k}$ of the true hypersurface Σ with the cell edges are computed by NEWTON iteration. The level-set function is approximated by a third-order polynomial based on the values of the level-set function ϕ_Σ and its gradient $\nabla\phi_\Sigma$, evaluated at the cell corners. If the hypersurface is parameterizable over some parameter set \mathcal{S}_Σ , i.e. $\Sigma = \{\mathbf{g}_\Sigma(\mathbf{t}) : \mathbf{t} \in \mathcal{S}_\Sigma\}$, the centroid of the polygon spanned by the edge intersections is projected onto \mathcal{S}_Σ to obtain $\hat{\mathbf{t}}_{\partial\Sigma} := \mathbf{g}_\Sigma^{-1}(\hat{\mathbf{x}}_{\partial\Sigma})$, with $\hat{\mathbf{x}}_{\partial\Sigma} = 1/N \sum_{k=1}^N \mathbf{x}_{\partial\Sigma, k}$ and $\mathbf{g}_\Sigma^{-1} : \mathbb{R}^d \mapsto \mathcal{S}_\Sigma$ surjective. The base point is then obtained as $\mathbf{x}_0 = \mathbf{g}_\Sigma(\hat{\mathbf{t}}_{\partial\Sigma})$. For hypersurfaces that are not parameterizable in the above sense, a metric projection dependent on the class of the respective hypersurface is applied. The principal curvatures κ_i and associated directions $\boldsymbol{\tau}_i$ define the approximated hypersurface Γ , whose intersections $\mathbf{x}_{\partial\Gamma, k}$ with the cell edges, after projection onto the tangential plane via $\mathcal{P}_\Gamma(\mathbf{x}) := [\boldsymbol{\tau}_1, \boldsymbol{\tau}_2]^\top (\mathbf{x} - \mathbf{x}_0)$, provide the vertices \mathbf{t}_k of the parameter set polygon $\mathcal{S}_\Gamma \approx \bigcup_k \mathcal{T}_k$; cf. again figure 6. Due to the polynomial character of the underlying equation, cf. subsection 2.5, it is possible to approximate the solution either by a variational formulation or by comparison of polynomial coefficients. In the latter case, the coefficients associated to the ansatz functions φ_k^a can be evaluated directly. The first case, i.e. the application of PETROV-GALERKIN approach, however requires to assemble a linear system, which is solved employing the LAPACK routines DGETRF and DGETRS. Numerical experiments have shown that for very small hypersurface patches ($|\Gamma| \leq 10^{-7}$)⁵, the system may become ill-posed. For those non-invertible matrices \mathbf{A}_Γ , the principal curvatures κ_i are set to zero, corresponding to a planar approximation, and the edge intersections $\mathbf{x}_{\partial\Gamma, k}$ are recomputed. After assembling the solution u , the rightmost expression of eq. (2) can be evaluated. The integral over the hypersurface is evaluated using eq. (4) on $\partial\Gamma = \bigcup_k \partial\Gamma_k$, where the details are given in subsection 3.1. A cell face \mathcal{F}_k with a non-zero contribution to eq. (2) is either intersected by Γ or interior (i.e., $\phi_\Gamma(\mathbf{x}) < 0 \quad \forall \mathbf{x} \in \mathcal{F}_k$), where in the first case the area is computed by standard quadrature. If the computed volume is negative or exceeds the volume of the containing cell, the curvatures κ_i are set to zero, and the edge intersections $\mathbf{x}_{\partial\Gamma, k}$ are recomputed as in the case of a non-invertible \mathbf{A}_Γ . This case will be referred to as *out of bounds* below.

⁴Note that due to the cell based application parallelization of this algorithm is trivial.

⁵This value is related to the tolerance employed in the root finding algorithm, where we used 10^{-6} .

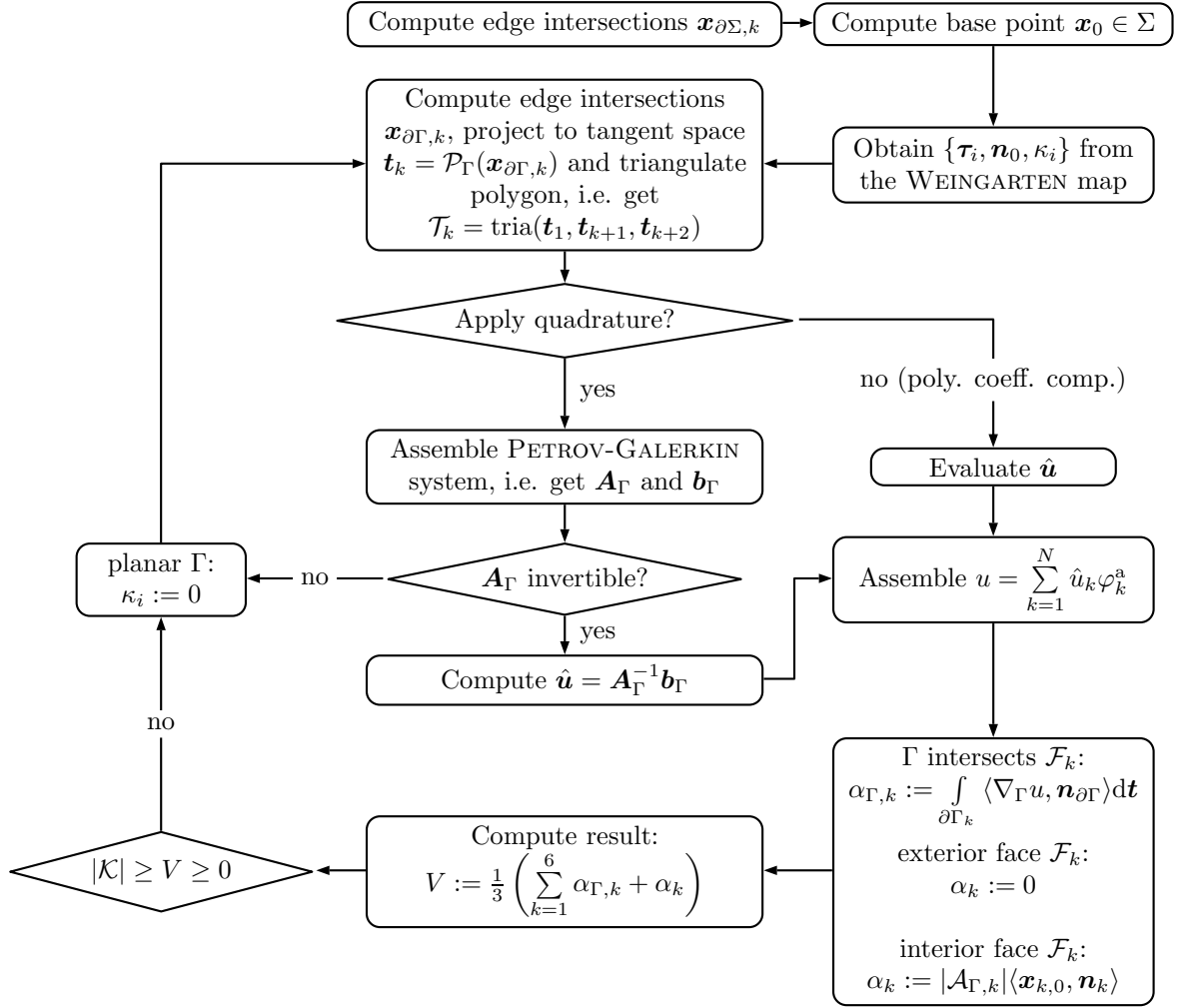


Figure 8: Flowchart of the numerical algorithm.

3.1 Numerical quadrature of curve integrals

The present subsection is concerned with the evaluation of integrals of the form $\int_{\partial\Gamma} \langle \nabla_\Gamma u, \mathbf{n}_{\partial\Gamma} \rangle dl$, where $u : \Gamma \mapsto \mathbb{R}$ is the numerical solution of eq. (22). As stated above, cf. figure 2, a boundary curve segment $\partial\Gamma_k = \partial\Gamma \cap \mathcal{F}_k$ contained in the rectangular face \mathcal{F}_k can be parameterized in two ways. Firstly, in terms of a height function over one of the edges of the face \mathcal{F}_k , i.e.

$$\partial\Gamma_k = \{\mathbf{g}_{\partial\Gamma,k}(\mu) : \mu \in \mathcal{S}_{\partial\Gamma,k}\} \quad \text{with} \quad \mathbf{g}_{\partial\Gamma,k} := \mathbf{x}_{0,k} + \mu \mathbf{b}_k + h_{\partial\Gamma,k}(\mu) \mathbf{n}_k, \quad (31)$$

where $\mathcal{S}_{\partial\Gamma,k}$ is the simply connected parameter domain of the height function. Alternatively, polar coordinates can be applied, yielding

$$\partial\Gamma_k = \{\mathbf{g}_{\partial\Gamma,k}(\mu) : \mu \in [0, \pi/2]\} \quad \text{with} \quad \mathbf{g}_{\partial\Gamma,k} := \mathbf{x}_{0,k} + r_{\partial\Gamma,k}(\mu) \mathbf{e}_r(\mu), \quad (32)$$

where $\mathbf{e}_r|_{\mu=0} = \mathbf{b}_k$ and $\mathbf{e}_r|_{\mu=\pi} = \mathbf{n}_k$. The latter representation is chosen if two adjacent edges of a face are intersected, whereas the height function is used in the case of opposing intersected edges. The polar representation is required to cover the case where $\partial\Gamma_k$ is not the graph of a function whose independent variable varies along an edge, cf. figure 4(a). Since we ultimately wish to perform quadrature operations on $\partial\Gamma_k$, the quadrature nodes $\mu_{k,i}$ need to be chosen carefully to ensure good approximation for strongly varying $r_{\partial\Gamma,k}$. The standard GAUSS-LEGENDRE nodes $\mu_{i,k} \in [0, \pi/2]$ are transformed via

$$\tilde{\mu}_{k,i} = \tan^{-1}(\alpha_k \tan \mu_{k,i}), \quad (33)$$

where α_k denotes the ratio of the distances of the interface intersection $\mathbf{x}_{0,k}$ to the base point $\mathbf{x}_{\partial\Gamma,k}$; cf. figure 9 for an illustration.

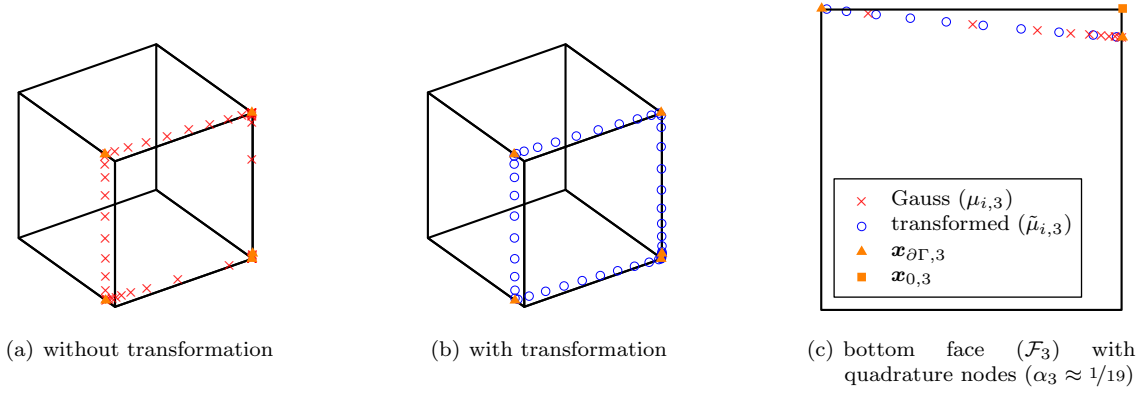


Figure 9: Exemplified quadrature nodes on boundary curve $\partial\Gamma$ with (\circ) and without (\times) application of transformation; cf. eq. (33).

The upcoming transformations are derived for the first case, their polar pendants can be obtained by analogous manner. First, note that the choice of the local coordinate system $\{\mathbf{b}_k, \mathbf{n}_k\}$ is not unique, in general. By equating the expressions in eq. (31) and eq. (9) and computing the appropriate inner products for $i \in \{1, 2\}$, one obtains

$$t_i = \langle \mathbf{x}_{0,k} - \mathbf{x}_0, \boldsymbol{\tau}_i \rangle + \mu \langle \mathbf{b}_k, \boldsymbol{\tau}_i \rangle + \langle \mathbf{n}_k, \boldsymbol{\tau}_i \rangle h_{\partial\Gamma,k} =: \alpha_i + \mu\beta_i + \gamma_i h_{\partial\Gamma,k}, \quad (34)$$

$$\frac{1}{2} (\kappa_1 t_1^2 + \kappa_2 t_2^2) = \langle \mathbf{x}_{0,k} - \mathbf{x}_0, \mathbf{n}_0 \rangle + \mu \langle \mathbf{b}_k, \mathbf{n}_0 \rangle + \langle \mathbf{n}_k, \mathbf{n}_0 \rangle h_{\partial\Gamma,k} =: \alpha_3 + \mu\beta_3 + \gamma_3 h_{\partial\Gamma,k}. \quad (35)$$

Inserting eq. (34) in eq. (35) and rearranging yields the implicit quadratic relation

$$c_{2,k} h_{\partial\Gamma,k}^2 + c_{1,k}(\mu) h_{\partial\Gamma,k} + c_{0,k}(\mu) = 0 \quad (36)$$

with coefficients

$$\begin{aligned} c_{0,k} &= \frac{\mu^2}{2} (\kappa_1 \beta_1^2 + \kappa_2 \beta_2^2) + \mu (\kappa_1 \alpha_1 \beta_1 + \kappa_2 \alpha_2 \beta_2 - \beta_3) + \frac{1}{2} (\kappa_1 \alpha_1^2 + \kappa_2 \alpha_2^2) - \alpha_3, \\ c_{1,k} &= \mu (\kappa_1 \beta_1 \gamma_1 + \kappa_2 \beta_2 \gamma_2) + \kappa_1 \alpha_1 \gamma_1 + \kappa_2 \alpha_2 \gamma_2 - \gamma_3, \\ c_{2,k} &= \frac{1}{2} (\kappa_1 \gamma_1^2 + \kappa_2 \gamma_2^2). \end{aligned} \quad (37)$$

Despite the possibility of explicitly calculating the roots of eq. (36), we prefer to apply a NEWTON algorithm. Also, the derivative of the height function $h_{\partial\Gamma,k}$ with respect to μ , which is required in eq. (40) below for the integral transformation, can be computed by differentiating eq. (36) and rearranging, i.e.

$$\frac{\partial h_{\partial\Gamma,k}}{\partial \mu} = -\frac{\partial_\mu c_{0,k} + h_{\partial\Gamma,k} \partial_\mu c_{1,k}}{2h_{\partial\Gamma,k} c_{2,k} + c_{1,k}}. \quad (38)$$

The boundary normal emerges from the projection of the face normal $\mathbf{n}_{\mathcal{F},k}$ onto the tangent space, i.e.

$$\mathbf{n}_{\partial\Gamma,k}(\mathbf{t}) = \frac{\mathbf{P}_\Gamma \mathbf{n}_{\mathcal{F},k}}{\|\mathbf{P}_\Gamma \mathbf{n}_{\mathcal{F},k}\|}. \quad (39)$$

Finally, the curve integral is transformed as

$$\int_{\partial\Gamma_k} \langle \nabla_\Gamma u, \mathbf{n}_{\partial\Gamma,k} \rangle(\mathbf{t}) dl = \int_{\mathcal{S}_{\partial\Gamma,k}} \langle \nabla_\Gamma u, \mathbf{n}_{\partial\Gamma,k} \rangle(\mathbf{g}_{\partial\Gamma,k}(\mu)) \sqrt{1 + \partial_\mu h_{\partial\Gamma,k}^2} d\mu, \quad (40)$$

where the numerical evaluation is, once again, carried out by standard GAUSS-LEGENDRE quadrature. Figure 10 illustrates the relevant quantities.

4 Numerical results

The present section gathers some numerical results for three classes of hypersurfaces, which are commonly encountered in the initial configuration of two-phase flow simulation: (i) ellipsoids with distinct and identical semi-axes (a, b, c) ,

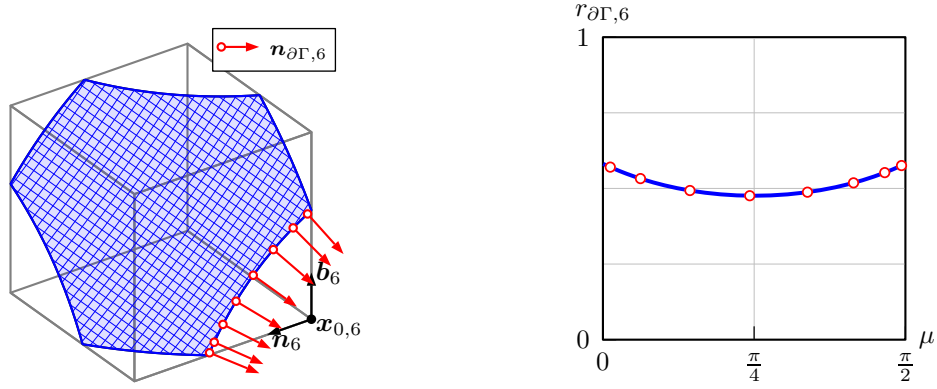


Figure 10: Relevant quantities for numerical quadrature of curve integrals, where the boundary normals are evaluated for $M = 8$ quadrature nodes on the parameter set $\mathcal{S}_{\partial\Gamma,6} = [0, \frac{\pi}{2}]$ and $\alpha_6 = 1$.

the latter of course resembling spheres. (ii) hypersurfaces with rotational symmetry along the z -axis, whose radius is a quadratic function of the z -coordinate and (iii) perturbed spheres with base radius R_0 and variance σ_0 .

Since the numerical evaluation of the original equation, cf. eq. (3), involves two significant distinguishable error sources, namely the approximation of the hypersurface and the numerical approximation of the variational problem, the convergence with increasing resolution is bounded by the approximation accuracy. Hence, due to the symmetry of local quadratic approximation of the hypersurface, one can obtain fourth-order convergence in space at most. The number of cells \mathcal{K}_i intersected by the hypersurface Σ is denoted N_Σ , which is not an input parameter. In figures 12 and 13, the computation of the referential error employs a discretization of the hypersurface parameter set \mathcal{S}_Σ into N_Σ^2 subdomains. In order to achieve comparability in terms of resolution, the errors produced by our algorithm are plotted over $\sqrt{N_\Sigma}$, approximately resembling the interface resolution per spatial dimension, i.e. $N_\Sigma^2 \sim N_\Sigma$.

4.1 Numerical setup

The domain $\mathcal{K} = [-1, 1]^3$ under consideration is evenly discretized by $N_{\mathcal{K}}$ cells per spatial dimension, where the center of volume coincides with the center of the domain. For both the PETROV-GALERKIN (PG) and the polynomial comparison (PC) approach, the number of ansatz functions is $N \in \{4, 9\}$, corresponding to products of even LEGENDRE polynomials up to and including second ($M = 2$) and fourth order ($M = 4$), respectively; cf. eq. (24). The GAUSS-LEGENDRE quadrature of eq. (22) is carried out using $(2M + 2)^2$ nodes per triangle, cf. eq. (23). For the quadrature on the boundary curve segments $\partial\Gamma_k$, cf. eq. (40), $2M + 6$ nodes are used. For all cases investigated below, there are no cells for which the coefficient matrix \mathbf{A}_Γ is non-invertible; cf. eq. (30) and the flowchart in figure 8. Moreover, for ellipsoids and hyperboloids of rotation no occurrences of *out-of-bounds* are detected, while table 3 provides the numbers for perturbed spheres.

4.2 Referential volumes

In order to separately analyze the error contribution of the local surface approximation, we compute the theoretical minimum error of the volume computation. The referential volumes are obtained as follows: the rectangular parameter set $\mathcal{S} = [\alpha_1, \beta_1] \times [\alpha_2, \beta_2]$ is discretized in $N_\mathcal{S} \times N_\mathcal{S}$ equally sized rectangular pairwise disjoint subdomains \mathcal{S}_{ij} , i.e. $\mathcal{S} = \bigcup_{i,j=1}^{N_\Sigma} \mathcal{S}_{ij}$ with

$$\mathcal{S}_{ij} = \left[\alpha_1 + \frac{\beta_1 - \alpha_1}{N_\Sigma}(i - 1), \alpha_1 + \frac{\beta_1 - \alpha_1}{N_\Sigma}i \right] \times \left[\alpha_2 + \frac{\beta_2 - \alpha_2}{N_\Sigma}(j - 1), \alpha_2 + \frac{\beta_2 - \alpha_2}{N_\Sigma}j \right]. \quad (41)$$

The approximate interface patch Γ_{ij} is obtained by TAYLOR expansion of the height function h_Σ around the respective center of \mathcal{S}_{ij} , providing $\{\kappa_i, \boldsymbol{\tau}_i, \mathbf{n}_0\}$. Next, we explicitly compute a set of $N_{\text{quad}}^2 = 64$ quadrature weights and nodes $\{(\omega_k, \mathbf{x}_k)\}_{ij}$ with $\mathbf{x}_k \in \Sigma_{ij}$ which is projected to the approximate parameter set space, yielding $\{(\omega_k, \mathbf{b}_k)\}_{ij}$. Finally, the approximate volume V_{ij}^Γ is computed by evaluating the approximate height functions, while the true volume V_{ij}^Σ is computed from the true height function, analytically where possible. For the hypersurfaces under consideration here,

table 2 gathers the relevant quantities. The global volume error then can be cast as

$$\mathcal{E}_V^{\text{ref}} := \left| 1 - \left(\sum_{i=1}^{N_S} \sum_{j=1}^{N_S} V_{ij}^\Gamma \right) \left(\sum_{i=1}^{N_S} \sum_{j=1}^{N_S} V_{ij}^\Sigma \right)^{-1} \right|, \quad (42)$$

i.e. eq. (42) resembles an "upper bound" for the accuracy of the numerical implementation.

Table 2: Analytical volume segments for hypersurfaces under consideration for the numerical experiments, where the evaluation is carried out analytically for ellipsoids and hyperboloids of rotation.

class	parameters	\mathcal{S}_Σ	V_{ij}^Σ
hlinehyperb. of rev.	$(r_0, \Delta r)$	$[0, 2\pi) \times [-1, 1]$	$\int_{z_i}^{z_{i+1}} \int_{\varphi_i}^{\varphi_{i+1}} \frac{(r_0 + \Delta r z^2)^2}{2} d\varphi dz$
ellipsoid	(a, b, c)	$[0, 2\pi) \times [0, \pi]$	$\frac{abc}{3} (\cos \theta_j - \cos \theta_{j-1}) (\varphi_{i+1} - \varphi_i)$
pert. sphere	(R_0, σ_0)	$[0, 2\pi) \times [0, \pi]$	$\frac{1}{3} \int_{\varphi_i}^{\varphi_{i+1}} \int_{\theta_j}^{\theta_{j+1}} R^3 \sin \theta d\theta d\varphi$

4.3 Ellipsoids

Figure 12 gathers the global numerical volume error for ellipsoids with different semi-axes, where the black and orange full circles denote the referential error of eq. (42) and the error obtained by linear approximation of the hypersurface, respectively. In general, the relative error decreases with increasing spatial resolution, commencing from between 10^{-3} and 10^{-4} for the lowest resolution of $N_\kappa = 10$ and reaching 10^{-8} for spheres and 10^{-7} for true ellipsoids, i.e. those with different semi-axes, respectively. For the latter the experimental order of convergence varies between 3.00 and 4.36, where in the cases presented here larger variations of curvatures do not necessarily produce lower orders of convergence; cf. figure 11.

For all cases considered here, the absolute error of the PETROV-GALERKIN approach lies approx. two orders of magnitude below the error induced by linear approximation, indicating the benefits of exploiting local curvature information. Also, the PETROV-GALERKIN approach outperforms the polynomial comparison for $N = 4$ ansatz functions. As figure 12 indicates, the polynomial comparison requires $N = 9$ ansatz functions (PC9) to produce results equivalent to (PG4). Polynomial comparison with $N = 4$ ansatz functions (PC4) in general exhibits second order convergence in space, with the absolute error being roughly one order of magnitude below the linear approximation. This is due to the non-local character of the weak formulation underlying the PETROV-GALERKIN approach, allowing for partial compensation of the higher order terms, which are neglected within the polynomial comparison. Moreover, increasing the number of ansatz functions to $N = 9$ (PG9) does not improve the accuracy of the PETROV-GALERKIN approach, implying that terms of fourth order in t_i do not contribute significantly to the solution $u(\mathbf{t}; \kappa_i)$, irrespective of the sign and value of the principal curvatures; in fact, the observations of this paragraph extend to all classes of hypersurfaces investigated in this section, see figures 13 and 15.

For the spherical case, cf. figure 12(d), the PETROV-GALERKIN approach produces the expected fourth order convergence. Also, there is virtually no difference between the PETROV-GALERKIN approach and the polynomial comparison, both for $N = 4$ and $N = 9$ ansatz functions. This is to be expected because the ansatz space \mathcal{F}_4^a already contains the analytical solution for $\kappa_1 = \kappa_2 = \kappa$, hence an expansion cannot increase accuracy, since $\mathcal{F}_9^a \supset \mathcal{F}_4^a$.

Let $\beta := c/a$ be the ratio of the smallest and largest semi-axis. Figure 11 depicts the experimental order of convergence as a function of $\beta \in [1/2, 95/100]$, comparing the uniform variation of one (*oblate*) and two (*prolate*) semi-axes. For both oblate and prolate ellipsoids, the experimental order of convergence is approx. four, virtually independent of β . For the oblate ellipsoid with $\beta = 3/5$, cf. figure 12(a), the experimental order of convergence for PG4 drops to 3 due to sporadic increments in the absolute error magnitude. However, since we obtain fourth order convergence in space for both smaller and larger values of β , we can deduce that this is caused by disadvantageous cancellation of local errors. An advantageous pronouncement of the aforementioned effect occurs for $N_\kappa = 20$ in PC9, where obtain an absolute error of approx. 10^{-8} , as compared to approx. 10^{-6} for $N_\kappa = 30$.

4.4 Hyperboloids of revolution

Hyperboloids of revolution can be described by level-set functions of type

$$\phi_\Sigma(\mathbf{x}; r_0, \Delta r) = x^2 + y^2 - (r_0 + \Delta r z^2)^2. \quad (43)$$

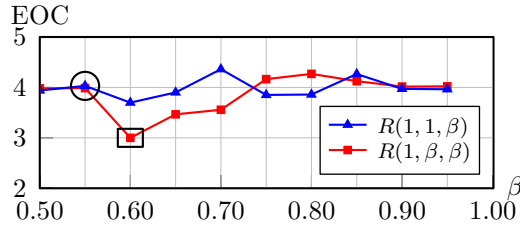


Figure 11: Experimental order of convergence of PG4 for $10 \leq N_{\mathcal{K}} \leq 100$ cells per spatial direction for oblate (\blacktriangle) and prolate (\blacksquare) ellipsoids over varying ratio of semi-axes ($R = 0.99$). Figure 12 below provides the underlying relative errors as a function of the spatial resolution $N_{\mathcal{K}}$, where the points marked by the square/circle correspond to ((b), (c)) / (a).

Figure 13 shows the referential, cf. eq. (42), and numerical global volume error for hyperboloids of revolution with different radius variations. The observations concerning the evolution of the global error basically correspond to those of the ellipsoids. At this point, it is worth noting that we obtain fourth order convergence for (globally) non-convex hypersurfaces, cf. figures 13(b) and (d).

4.5 Perturbed spheres

Perturbed spheres can be described by level-set functions in spherical coordinates $\mathbf{r} := [r, \varphi, \theta]^T$ of type

$$\phi_{\Sigma}(\mathbf{r}; R_0, \sigma_0) = r^2 - R^2(\varphi, \theta; R_0, \sigma_0), \quad (44)$$

where the description of the radius R employs tesseral spherical harmonics up to and including order $L \in \mathbb{N}$, i.e.

$$R^3 = \sum_{l=0}^L \sum_{m=-l}^{m=l} c_l^m \mathcal{Y}_l^m(\varphi, \theta). \quad (45)$$

The reason for expanding the third power of the radius instead of the radius itself is that the computation of the enclosed volume is considerably simplified, because $|\text{dom}(\Sigma)| = c_0^0 \sqrt{4\pi}/3$. Moreover, to ensure continuity of the polar derivatives at the poles, modes with $m = \pm 1$ are excluded, i.e. we enforce $c_l^{\pm 1} \equiv 0$; cf. C for details. The $(L+1)^2 - 2L$ coefficients $c_l^m \sim \mathcal{N}(0, \sigma_0)$ are computed by the BOX-MULLER method, i.e.

$$c_l^m = \begin{cases} \sqrt{4\pi} R_0^3 & l = 0 \\ \sqrt{\sigma_0 \sqrt{-2 \log \gamma_1} \cos(2\pi\gamma_2)} & l > 0 \end{cases} \quad \text{with} \quad \gamma_{1,2} \sim \mathcal{U}(0, 1). \quad (46)$$

In general, the observations concerning convergence and absolute error magnitude which have been established in 4.3 hold for the perturbed spheres as well. However, there are two characteristic differences. First, it is worth noting that the referential errors, cf. eq. (42), obtained from direct quadrature with $N_{\text{quad}} = 64$ nodes (see figures 15(a), (c) and (e)) are larger than those obtained by application of our approach (excluding PC4), indicating its performance for locally non-convex hypersurfaces. If the deviation from the sphere is small, which is the case for $L = 3$, the polynomial comparison performs better in terms of absolute error. Second, while there were no cells whose volume fractions were out of bounds in 4.3 to 4.4, this phenomenon occurs for perturbed spheres; cf. table 3. However, in the cases investigated here, the maximum number of those cells is three (obtained for $L = 9$ with PC9), corresponding to 0.01% of the intersected cells; the affected cells share the property of having volume fractions close to 1 or 0⁶; cf. figure 14 for details. This exceedance can be explained as follows: if all intersection points \mathbf{x}_{Σ} are located in the very vicinity of corners, as illustrated in figure 14, even small values of $d_{\mathcal{K}\kappa_i}$ can cause $\partial\Gamma \not\subset \mathcal{K}$. In other words, even small relative curvatures of the boundary curve potentially cause the latter to leave the cell under consideration. However, due to the aforementioned prerequisites concerning the intersection, this effect is expected to occur relatively rarely; cf. again table 3.

5 Conclusion

We have introduced an algorithm capable of computing volumes of domains which emerge from the intersection of cuboids and implicitly given hypersurfaces, where the novelty of the approach consists in the explicit exploitation of

⁶Note that the inverse relation is not true, i.e. cells with volume fractions close to 0 or 1 are generally not affected.

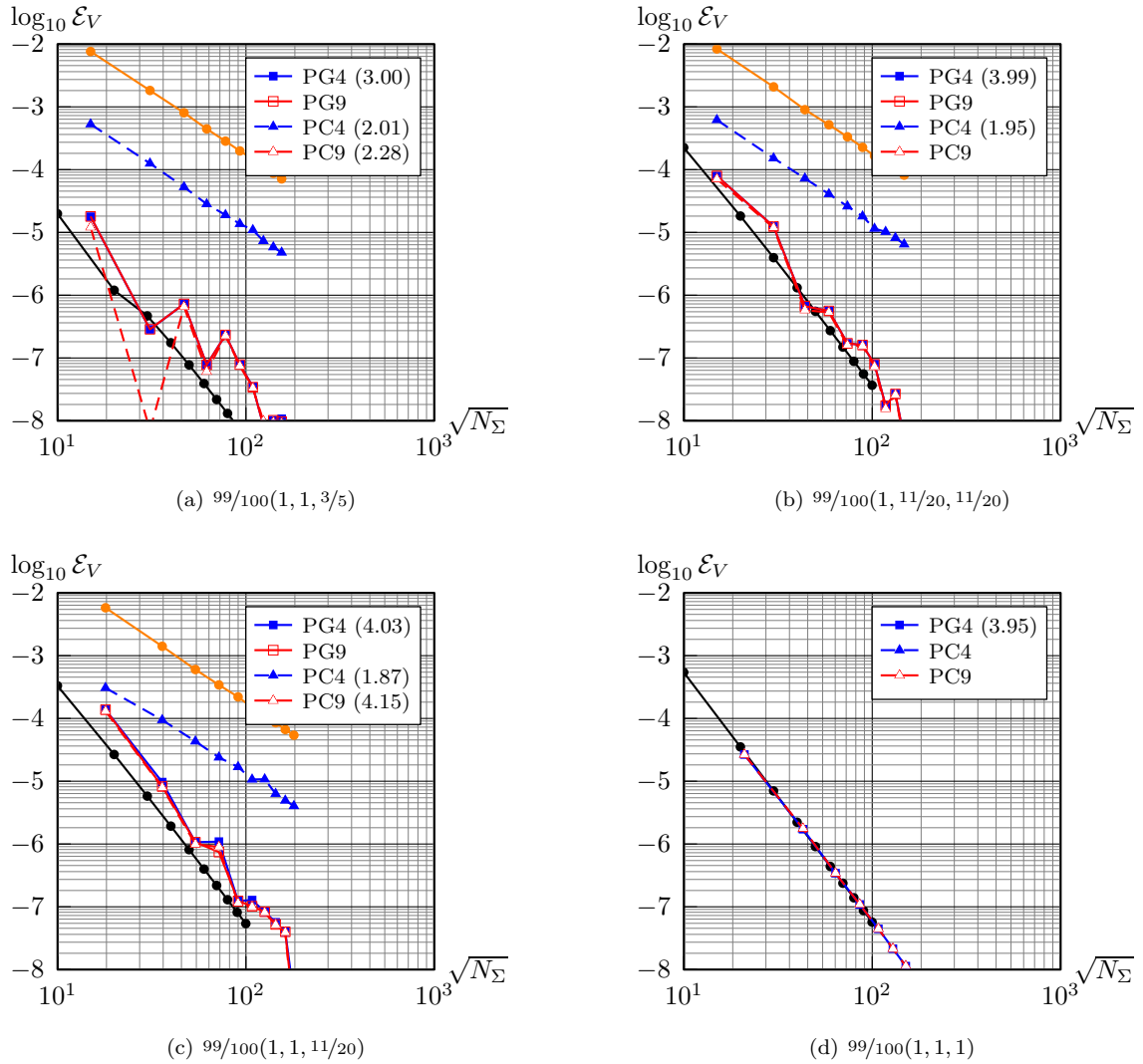
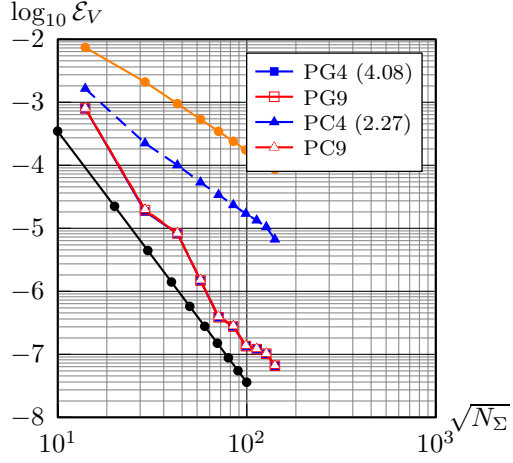


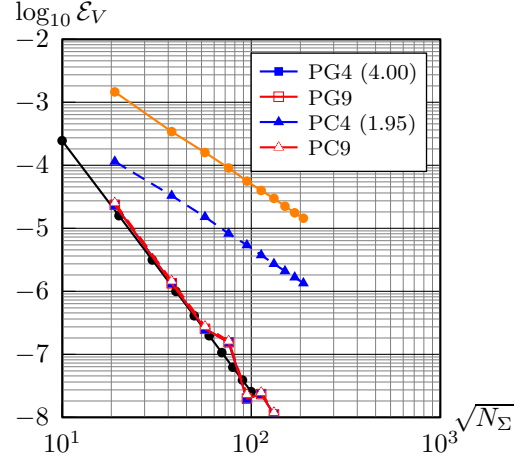
Figure 12: Volume error (ellipsoids; subtitles denote semi-axes; number in brackets denote the EOC) over number of intersected cells N_Σ with referential errors (\bullet : eq. (42) combined with table 2, \circ : linear approximation of hypersurface). (PG) denotes the results obtained with the PETROV-GALERKIN approach, (PC) refers to polynomial comparison.

curvature information, i.e. principal curvatures and axes, in combination with the application of surface divergence theorem, where the solution of the emerging PDE is approximated by means of a PETROV-GALERKIN ansatz. The following main conclusions are drawn:

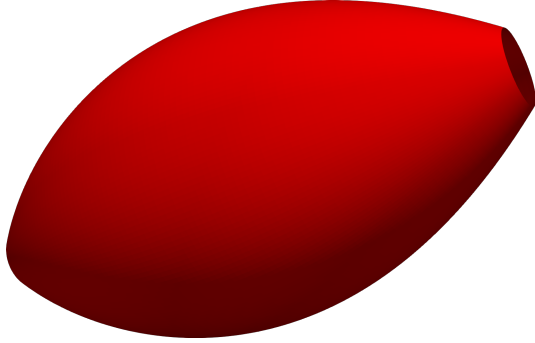
1. The local approximation of second order, exploiting geometrical (i.e. principal curvature) information from the WEINGARTEN map, allows to obtain fourth-order convergence with spatial resolution. For all cases considered here, the absolute error is approximately three orders of magnitude below the error obtained by linear approximation of the hypersurface.
2. Fourth-order convergence is obtained for both convex and (globally and locally) non-convex hypersurfaces.
3. The proposed PETROV-GALERKIN approach outperforms the polynomial comparison for an equal number of ansatz functions in terms of the absolute error, on average by one order of magnitude. Moreover, the results are robust with respect to the size of hypersurface patches, corresponding to the size of the parameter domains of the quadrature; cf. figure 17 for an illustration.
4. If (i) the principal curvatures are identical or (ii) one of the principal curvatures is zero, there is an analytical solution to the LAPLACE-BELTRAMI equation, which allows to compute the volume integrals exactly (with respect to the approximated hypersurface). This also considerably reduces the computational effort.



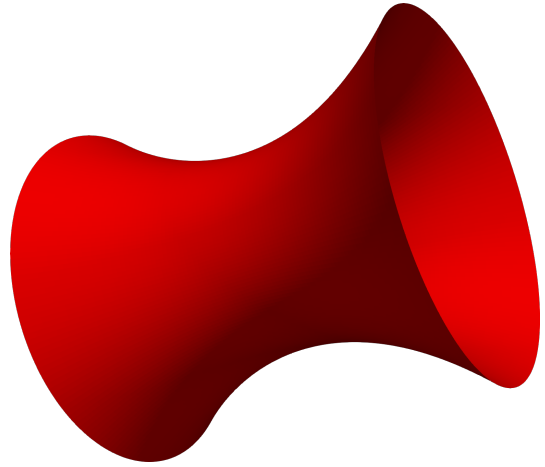
(a) $(\pi/6, -2/5)$



(b) $(\pi/6, 2/5)$



(c) $(\pi/6, -2/5)$



(d) $(\pi/6, 2/5)$

Figure 13: Volume error (hyperboloid of rotation; subtitles correspond to the parameters in table 2) over number of intersected cells N_Σ with referential errors (\bullet : eq. (42) combined with table 2, \circ : linear approximation of hypersurface) with illustrations.

In an upcoming paper, the authors will extend the numerical methods presented above for other right-hand sides of eq. (3), especially for polynomials and constants, including the computation of surface area as an important special case.

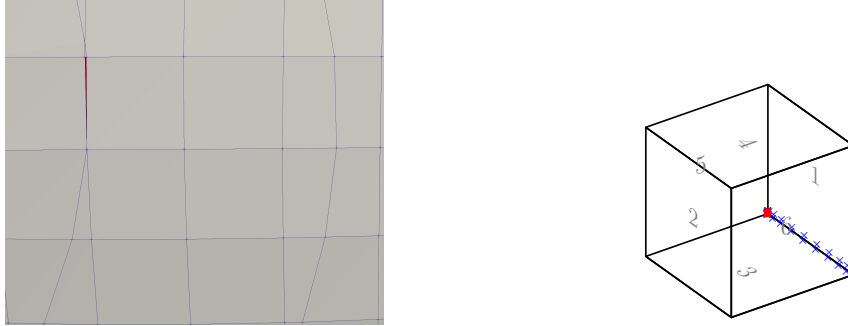
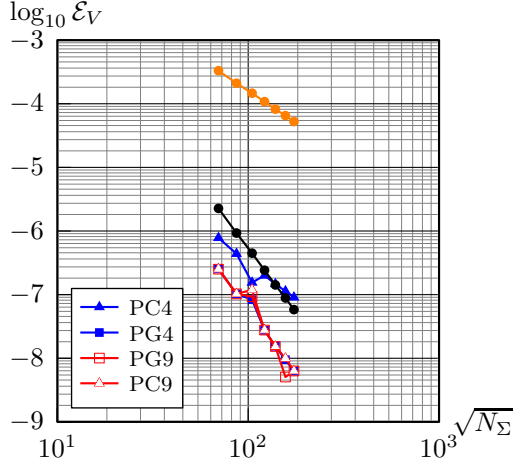


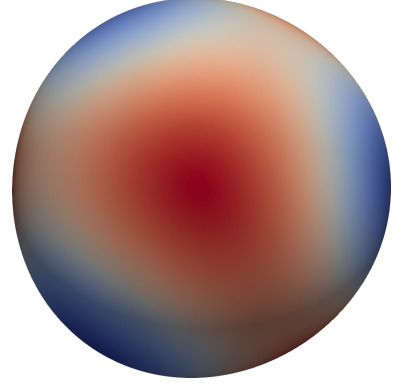
Figure 14: Left: surface mesh (red: out-of-bounds cells) for $L = 9$ and $N_{\mathcal{K}} = 90$ (PG4 result: -6.09×10^{-11} and -9.45×10^{-8}); right: cell (volume 1.097×10^{-5}) with hypersurface intersections \mathbf{x}_{Σ} (■) and quadrature nodes $\mathbf{x}_{\partial\Gamma}$ (×); cf. table 3.

Table 3: Number of interface cells of perturbed sphere for which $f_k \notin [0, 1]$ (*out-of-bounds*; cf. the flowchart in figure 8) and total number of intersected cells N_{Σ} over number of cells per spatial dimension $N_{\mathcal{K}}$. Note that the lowest possible resolution is $N_{\mathcal{K}} = 40$.

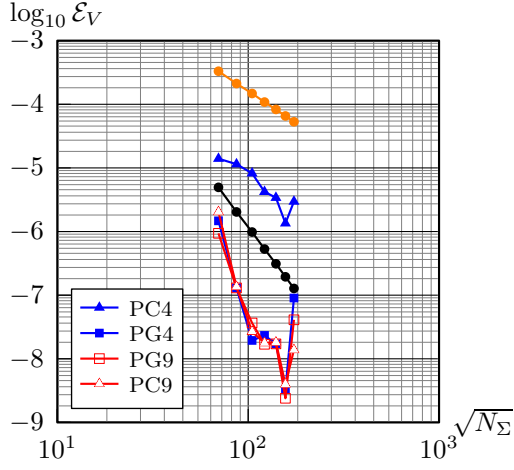
$N_{\mathcal{K}}$	$L = 3$				$L = 6$				$L = 9$						
	N_{Σ}	PG4	PG9	PC4	PC9	N_{Σ}	PG4	PG9	PC4	PC9	N_{Σ}	PG4	PG9	PC4	PC9
40	4820	0	0	0	0	4840	1	0	1	1	4996	1	0	1	0
50	7524	0	0	0	0	7566	0	0	0	0	7772	0	1	0	1
60	10870	1	1	1	0	10900	0	0	0	0	11250	1	2	2	1
70	14790	0	0	0	0	14838	0	0	0	0	15324	0	0	1	2
80	19302	0	0	0	0	19366	0	0	0	0	19992	1	2	1	3
90	24450	0	0	0	0	24508	0	0	0	0	25290	0	0	0	0
100	30163	0	0	0	0	30267	1	2	0	2	31206	0	1	0	1



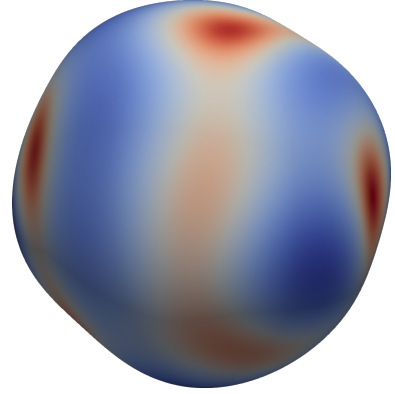
(a) rel. volume error



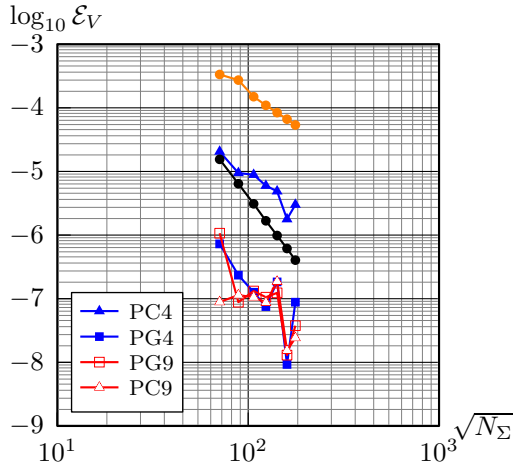
(b) $\kappa_1 + \kappa_2 = 2\kappa_\Sigma \in [-2.7, -2.2]$



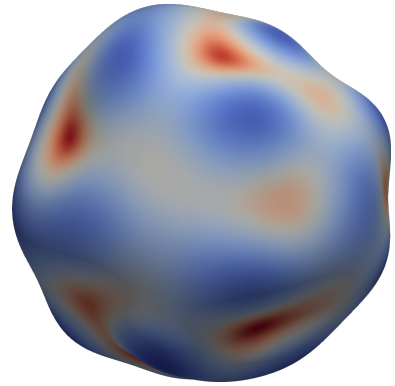
(c) rel. volume error



(d) $\kappa_1 + \kappa_2 = 2\kappa_\Sigma \in [-4.3, 0.25]$



(e) rel. volume error



(f) $\kappa_1 + \kappa_2 = 2\kappa_\Sigma \in [-7, 12]$

Figure 15: Volume error (perturbed sphere with $R_0 = 0.8$ and $\sigma_0 = 5 \times 10^{-4}$; top to bottom row: $L \in \{3, 6, 9\}$) over number of intersected cells N_Σ with referential errors (\bullet : eq. (42) combined with table 2, \circ : linear approximation of hypersurface) with illustrations. The blue (red) regions in (f) correspond to negative (positive) mean curvature $2\kappa_\Sigma = \kappa_1 + \kappa_2$.

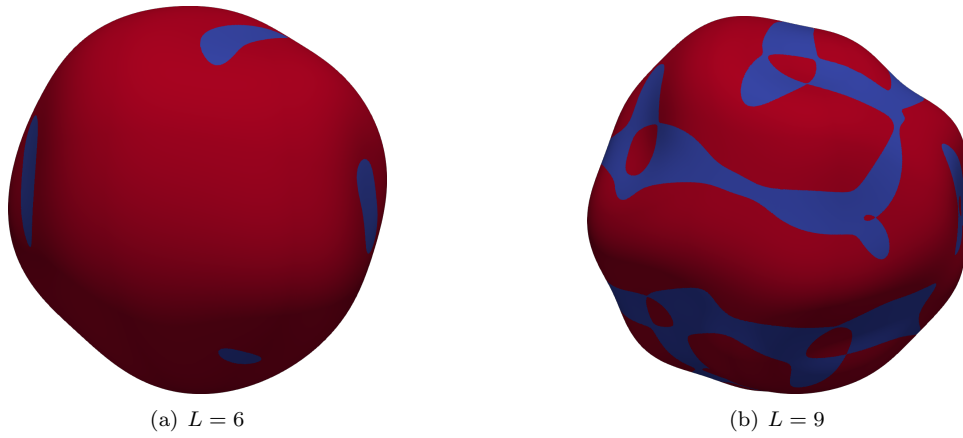


Figure 16: ((a),(b)): convexity index $\text{sign}(\kappa_1 \kappa_2)$ (red: 1, blue: -1) for perturbed spheres with $L \in \{6, 9\}$ evaluated on an evenly spaced discretization (2000×1000) of the parameter domain \mathbb{S} .

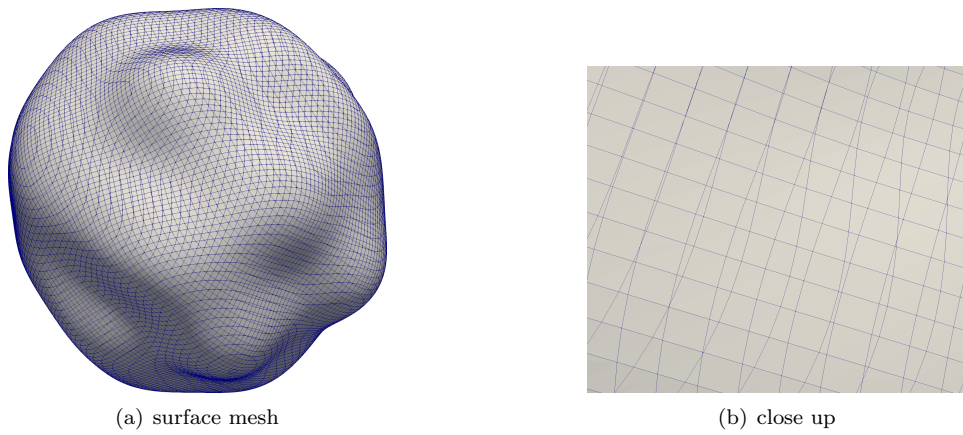


Figure 17: Surface mesh for $L = 9$ where the cuboidal domain was discretized in $N_{\mathcal{K}} = 100$ cells per spatial direction. The close up displays hypersurface patches with a wide range of sizes.

References

- S. Bna, S. Manservigi, R. Scardovelli, P. Yecko, and S. Zaleski. Numerical integration of implicit functions for the initialization of the VOF function. *Computers & Fluids*, 113:42–52, 2015.
- David Gilbarg and Neil S. Trudinger. *Elliptic Partial Differential Equations of Second Order*. Classics in Mathematics. Springer Berlin, 2001.
- C. W. Hirt and B. D. Nichols. Volume of fluid (vof) method for the dynamics of free boundaries. *Journal of Computational Physics*, 39:201–225, 1981.
- Wolfgang Kühnel. *Differential geometry. Curves-Surfaces-Manifolds*, volume 2. American Mathematical Society, 2005.
- Chohong Min and Frederic Gibou. Geometric integration over irregular domains with application to level-set methods. *Journal of Computational Physics*, 226:1432–1443, 2007.
- Björn Müller, Florian Kummer, Martin Oberlack, and Yongqi Wang. Simple multidimensional integration of discontinuous functions with application to level set methods. *International Journal for Numerical Methods in Engineering*, 92:637–651, 2012.
- Björn Müller, Florian Kummer, and Martin Oberlack. Highly accurate surface and volume integration on implicit domains by means of moment-fitting. *International Journal for Numerical Methods in Engineering*, 96:512–528, 2013.
- Jan Prüss and Gieri Simonett. *Moving Interfaces and Quasilinear Parabolic Evolution Equations*. Springer, 2016. ISBN 978-3-319-27698-4.
- Jan Prüss and Gieri Simonett. On the manifold of closed hypersurfaces in \mathbb{R}^N . *Discrete and continuous dynamical systems*, 33(11&12):5407–5428, 2013.
- Peter Smereka. The numerical approximation of a delta function with application to level set methods. *Journal of Computational Physics*, 211:77–90, 2006.
- Xin Wen. High order numerical methods to a type of delta function integrals. *Journal of Computational Physics*, 226:1952–1967, 2007.
- Xin Wen. High order numerical methods to two-dimensional delta function integrals in level set methods. *Journal of Computational Physics*, 228:4273–4290, 2009.
- Xin Wen. High order numerical methods to three dimensional delta function integrals in level set methods. *SIAM Journal of Scientific Computing*, 32:1288–1309, 2010.

ACKNOWLEDGEMENT

The work of J. Kromer has been partly supported by the **Excellence Initiative of the German Federal and State Governments** and the **Graduate School of Computational Engineering** at Technical University Darmstadt, Germany. Also, the authors gratefully acknowledge financial support provided by the German Research Foundation (DFG) within the scope of SFB-TRR 75.

A A brief review of basic facts from differential geometry

Prüss and Simonett [2013] give a survey on smooth closed hypersurfaces embedded in \mathbb{R}^N , including rigorous mathematical statements on the associated operators, fundamental forms and other geometrical properties. The present subsection heavily draws from their work. Here, however, we only reproduce those results needed within the scope of this work. For further mathematical details, the interested reader is referred to, e.g., the book of Kühnel [2005].

Let Σ be a hypersurface patch of class \mathcal{C}^2 confined by $\mathcal{K} \subset \mathbb{R}^d$ with $d \in \{2, 3\}$, which is given via the zero iso-contour of a level-set ϕ , i.e.

$$\Sigma = \{\mathbf{x} \in \mathcal{K} : \phi(\mathbf{x}) = 0\} \quad \text{with normal} \quad \mathbf{n}_\Sigma := \frac{\nabla \phi}{\|\nabla \phi\|}. \quad (47)$$

Recall that we have $\partial\mathcal{K} \supset \partial\Sigma \neq \emptyset$, by assumption; cf. figure 2.

Curvatures, first & second fundamental form For any point $\mathbf{x}_0 \in \Sigma$ with outer unit normal \mathbf{n}_Σ , there is a ball $\mathcal{B}_R(\mathbf{x}_0) \subset \mathbb{R}^d$ with radius R and a diffeomorphism $\Phi : \mathcal{B}_R(\mathbf{x}_0) \mapsto \mathcal{U} \subset \mathbb{R}^d$, such that $\mathcal{U} \ni \Phi(\mathbf{x}_0) = \mathbf{0}$ and

$$\Phi^{-1}(\mathcal{U} \cap (\mathbb{R}^{d-1} \times \{0\})) = \Phi^{-1}(\mathcal{S}_\Sigma \times \{0\}) = \mathcal{B}_R(\mathbf{x}_0) \cap \Sigma. \quad (48)$$

The implication of eq. (48) is that in the vicinity of \mathbf{x}_0 , i.e. for $\|\mathbf{x} - \mathbf{x}_0\| \leq R$, the hypersurface can be parametrized over some (open) parameter set $\mathcal{S}_\Sigma \subset \mathbb{R}^{d-1}$, i.e.

$$\Sigma \cap \mathcal{B}_R(\mathbf{x}_0) = \mathbf{g}(\mathcal{S}_\Sigma; \mathbf{x}_0) \quad \text{with} \quad \mathbf{g}(\mathbf{t}; \mathbf{x}_0) := \Phi^{-1}(\mathbf{t}, 0) \quad \text{and} \quad \mathbf{t} = \sum_{i=1}^{d-1} t_i \mathbf{e}_i; \quad (49)$$

cf. figure 18 for an illustration. The (covariant) tangent space T_Σ attached to \mathbf{x}_0 is spanned by

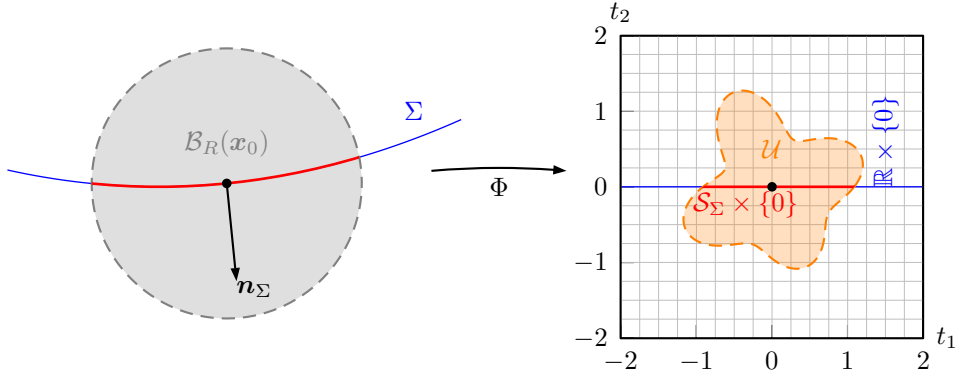


Figure 18: Illustration of the implicit function theorem for $\Sigma \subset \mathbb{R}^2$.

$$\boldsymbol{\nu}_i := \frac{\partial \mathbf{g}}{\partial t_i}(\mathbf{t}; \mathbf{x}_0) \quad \text{for} \quad 1 \leq i \leq d-1, \quad (50)$$

where $\langle \boldsymbol{\nu}_i, \mathbf{n}_\Sigma \rangle \equiv 0$, but, in general, $\|\boldsymbol{\nu}_i\| \neq 1$ and $\langle \boldsymbol{\nu}_i, \boldsymbol{\nu}_j \rangle \neq 0$. Analogously, $\boldsymbol{\nu}_{ij}$ denotes the second derivatives. Employing the EINSTEIN summation convention, the *first* and *second fundamental form*, respectively, can be written as

$$\mathbf{G}(\mathbf{x}_0) := \langle \boldsymbol{\nu}_i, \boldsymbol{\nu}_j \rangle \mathbf{e}_i \otimes \mathbf{e}_j \quad \text{and} \quad \mathbf{L}(\mathbf{x}_0) := \langle \mathbf{n}_\Sigma, \boldsymbol{\nu}_{ij} \rangle \mathbf{e}_i \otimes \mathbf{e}_j. \quad (51)$$

The eigenvalues $\{\kappa_i\} \subset \mathbb{R}^{d-1}$ of the WEINGARTEN map $\mathbf{W}(\mathbf{x}_0) := \mathbf{G}^{-1}\mathbf{L}$, also called *shape matrix* of Σ , correspond to the principal curvatures of the hypersurface at \mathbf{x}_0 . The associated eigenvectors $\boldsymbol{\tau}_i^0 \in \mathbb{R}^{d-1}$ provide the local directions of principal curvature, whose global pendant is obtained via $\boldsymbol{\tau}_i := \langle \boldsymbol{\tau}_i^0, \mathbf{e}_k \rangle \boldsymbol{\nu}_k$ and normalization. Note that $\langle \boldsymbol{\tau}_i, \boldsymbol{\tau}_j \rangle = \delta_{ij}$ as well as $\langle \boldsymbol{\tau}_i, \mathbf{n}_\Sigma \rangle = 0$, i.e. $\{\boldsymbol{\tau}_i, \mathbf{n}_\Sigma\}(\mathbf{x}_0)$ forms an orthonormal system and $T_\Sigma(\mathbf{x}_0) = \text{span}(\boldsymbol{\tau}_i)$.

Surface gradient & surface divergence Let $f : \Sigma \mapsto \mathbb{R}$ be a continuously differentiable field. Assume for the moment that the full gradient ∇f exists. Then, the surface gradient can be understood as the projection of ∇f onto the tangent space $T_\Sigma(\mathbf{x}_0)$, i.e.

$$\nabla_\Sigma f = (\mathbf{I} - \mathbf{n}_\Sigma \otimes \mathbf{n}_\Sigma) \nabla f = \frac{df}{d\boldsymbol{\tau}_1} \boldsymbol{\tau}_1 + \frac{df}{d\boldsymbol{\tau}_2} \boldsymbol{\tau}_2. \quad (52)$$

Note that left multiplication with $\mathbf{P}_\Sigma := \mathbf{I} - \mathbf{n}_\Sigma \otimes \mathbf{n}_\Sigma$ corresponds to a projection onto the tangent plane $T_\Sigma(\mathbf{x}_0)$. Following Gilbarg and Trudinger [2001], the lack of definition of the normal component can be eliminated by an extension of the definition, i.e. $f(\mathbf{x} \pm \epsilon \mathbf{n}_\Sigma) = f(\mathbf{x})$ for $\mathbf{x} \in \Sigma$ and $\mathbb{R} \ni \epsilon \ll 1$. Hence, within a tubular neighborhood of thickness 2ϵ , the function value is extended to be constant along a normal deviation from the hypersurface. In the remainder of this paper, we assume any function mapping from the hypersurface Σ to be extensible in this way. Then, the derivative in normal direction indeed becomes zero, since

$$\frac{df}{d\mathbf{n}_\Sigma} = \lim_{\epsilon \rightarrow 0} \frac{f(\mathbf{x} + \epsilon \mathbf{n}_\Sigma) - f(\mathbf{x})}{\epsilon} \equiv 0. \quad (53)$$

By analogous arguments, one obtains the surface divergence of a vector field $\mathbf{f} : \Sigma \mapsto \mathbb{R}^d$ as

$$\operatorname{div}_\Sigma \mathbf{f} = \operatorname{tr}(\mathbf{P}_\Sigma \nabla \mathbf{f}) = \left\langle \frac{d\mathbf{f}}{d\boldsymbol{\tau}_i}, \boldsymbol{\tau}_i \right\rangle, \quad (54)$$

i.e. the surface divergence is the trace of tangential projection of the full gradient. For a differentiable tangential vector field $\mathbf{f} : \Sigma \mapsto T_\Sigma$, especially including the case $\mathbf{f} = \nabla_\Sigma f$, the (surface) divergence theorem reads

$$\int_\Sigma \operatorname{div}_\Sigma \mathbf{f} \, d\mathbf{o} = \int_{\partial\Sigma} \langle \mathbf{f}, \mathbf{n}_{\partial\Sigma} \rangle \, dl. \quad (55)$$

For later application within the variational formulation, note that two scalar functions $f, g : \Sigma \mapsto \mathbb{R}$ fulfill

$$\int_\Sigma g \Delta_\Sigma f \, d\mathbf{o} = \int_{\partial\Sigma} g \langle \nabla_\Sigma f, \mathbf{n}_{\partial\Sigma} \rangle \, dl - \int_\Sigma \langle \nabla_\Sigma f, \nabla_\Sigma g \rangle \, d\mathbf{o}, \quad (56)$$

where the LAPLACE-BELTRAMI operator Δ_Σ is introduced in subsection 2.3.

B Comparison of polynomials

The first three elements of the coefficient vector $\hat{\mathbf{u}}$, where \hat{u}_{ij} corresponds to $t_1^{2i} t_2^{2j} \left(1 + \kappa_1^2 t_1^2 + \kappa_2^2 t_2^2\right)^{\frac{1}{2}}$, resulting from the polynomial comparison, cf. subsection 2.5, are

$$\begin{aligned} \hat{u}_{00} = \frac{1}{3465D} & \left[72544885875\kappa_1^{25} + 4193272314000\kappa_1^{24}\kappa_2 - 2577212786610\kappa_1^{23}\kappa_2^2 \right. \\ & - 26658698588694\kappa_1^{22}\kappa_2^3 - 57357128755944\kappa_1^{21}\kappa_2^4 + 336181054285530\kappa_1^{20}\kappa_2^5 \\ & + 41714627579527946\kappa_1^{19}\kappa_2^6 + 362007665932049430\kappa_1^{18}\kappa_2^7 \\ & + 1974693936115434347\kappa_1^{17}\kappa_2^8 + 8690216675233737542\kappa_1^{16}\kappa_2^9 \\ & + 18169798309454346220\kappa_1^{15}\kappa_2^{10} + 17997237348869644964\kappa_1^{14}\kappa_2^{11} \\ & + 8400471266096489992\kappa_1^{13}\kappa_2^{12} + 7621880627263011268\kappa_1^{12}\kappa_2^{13} \\ & + 18731291856940517620\kappa_1^{11}\kappa_2^{14} + 20016198248735780204\kappa_1^{10}\kappa_2^{15} \\ & + 16084926436271498425\kappa_1^9\kappa_2^{16} + 4111980253565015324\kappa_1^8\kappa_2^{17} \\ & - 9815326789142415706\kappa_1^7\kappa_2^{18} - 6784297128026141358\kappa_1^6\kappa_2^{19} \\ & - 1393140036723497824\kappa_1^5\kappa_2^{20} - 146622851045506110\kappa_1^4\kappa_2^{21} \\ & - 12737928185209566\kappa_1^3\kappa_2^{22} + 250947833147550\kappa_1^2\kappa_2^{23} \\ & \left. + 7442937203625\kappa_1\kappa_2^{24} + 5318812248750\kappa_2^{25} \right], \quad (57) \end{aligned}$$

$$\hat{u}_{10} = \frac{-1}{2130D} \left[72544885875\kappa_1^{27} + 3830547884625\kappa_1^{26}\kappa_2 - 22099585675860\kappa_1^{25}\kappa_2^2 \right]$$

$$\begin{aligned}
& + 64209322185606\kappa_1^{24}\kappa_2^3 - 206549792452944\kappa_1^{23}\kappa_2^4 \\
& + 1517363124557580\kappa_1^{22}\kappa_2^5 + 30461018702009246\kappa_1^{21}\kappa_2^6 \\
& + 109446918326844930\kappa_1^{20}\kappa_2^7 + 815480671742008547\kappa_1^{19}\kappa_2^8 \\
& + 1495391079214882517\kappa_1^{18}\kappa_2^9 + 4399306375420376470\kappa_1^{17}\kappa_2^{10} \\
& + 11540162436209873564\kappa_1^{16}\kappa_2^{11} + 1587688881052595192\kappa_1^{15}\kappa_2^{12} \\
& + 15758705774985074368\kappa_1^{14}\kappa_2^{13} + 9058115615694138220\kappa_1^{13}\kappa_2^{14} \\
& + 14577128661181516004\kappa_1^{12}\kappa_2^{15} + 8744727214400259625\kappa_1^{11}\kappa_2^{16} \\
& + 28905224435990940299\kappa_1^{10}\kappa_2^{17} + 2594680716262097144\kappa_1^9\kappa_2^{18} \\
& + 7186618173791294142\kappa_1^8\kappa_2^{19} - 9947751822646978024\kappa_1^7\kappa_2^{20} \\
& - 6203435202180262860\kappa_1^6\kappa_2^{21} - 828643056358660266\kappa_1^5\kappa_2^{22} \\
& - 64844425789431750\kappa_1^4\kappa_2^{23} + 1826532320191425\kappa_1^3\kappa_2^{24} \\
& - 63336193160625\kappa_1^2\kappa_2^{25} + 26594061243750\kappa_1\kappa_2^{26} \Big], \tag{58}
\end{aligned}$$

$$\begin{aligned}
\hat{u}_{01} = \frac{-1}{2130D} & \Big[362724429375\kappa_1^{26}\kappa_2 + 19594917775125\kappa_1^{25}\kappa_2^2 - 86674748460300\kappa_1^{24}\kappa_2^3 \\
& + 146615450910390\kappa_1^{23}\kappa_2^4 - 1207840768860744\kappa_1^{22}\kappa_2^5 \\
& + 11196251748762756\kappa_1^{21}\kappa_2^6 + 252896928659490030\kappa_1^{20}\kappa_2^7 \\
& + 1200927891952953746\kappa_1^{19}\kappa_2^8 + 7556833261950904455\kappa_1^{18}\kappa_2^9 \\
& + 15745185870149404097\kappa_1^{17}\kappa_2^{10} + 15147291587893508942\kappa_1^{16}\kappa_2^{11} \\
& + 10693380694498241020\kappa_1^{15}\kappa_2^{12} + 9860412201147581864\kappa_1^{14}\kappa_2^{13} \\
& + 18073647507342869392\kappa_1^{13}\kappa_2^{14} + 13060950214817275468\kappa_1^{12}\kappa_2^{15} \\
& + 26071491078811756420\kappa_1^{11}\kappa_2^{16} - 4777045933690144771\kappa_1^{10}\kappa_2^{17} \\
& + 3674918930866985575\kappa_1^9\kappa_2^{18} - 9858935048252420176\kappa_1^8\kappa_2^{19} \\
& - 1260715003218935506\kappa_1^7\kappa_2^{20} - 727484776891384608\kappa_1^6\kappa_2^{21} \\
& - 577234908550047124\kappa_1^5\kappa_2^{22} - 81527477422926810\kappa_1^4\kappa_2^{23} \\
& - 14557017568197366\kappa_1^3\kappa_2^{24} + 319602838556925\kappa_1^2\kappa_2^{25} \\
& - 19151124040125\kappa_1\kappa_2^{26} + 5318812248750\kappa_2^{27} \Big], \tag{59}
\end{aligned}$$

with the common factor

$$\begin{aligned}
D = & 942141375\kappa_1^{28} + 50895890325\kappa_1^{27}\kappa_2 - 224230144725\kappa_1^{26}\kappa_2^2 \\
& + 598532006835\kappa_1^{25}\kappa_2^3 - 2428874075520\kappa_1^{24}\kappa_2^4 + 16349986503270\kappa_1^{23}\kappa_2^5 \\
& + 427125623057490\kappa_1^{22}\kappa_2^6 + 2231665401399570\kappa_1^{21}\kappa_2^7 + 14828318817700617\kappa_1^{20}\kappa_2^8 \\
& + 44864797857680423\kappa_1^{19}\kappa_2^9 + 119751294597828609\kappa_1^{18}\kappa_2^{10} + 214219532483111305\kappa_1^{17}\kappa_2^{11} \\
& + 237484900845042006\kappa_1^{16}\kappa_2^{12} + 227521098241347780\kappa_1^{15}\kappa_2^{13} + 193178681355432300\kappa_1^{14}\kappa_2^{14} \\
& + 273867280881223980\kappa_1^{13}\kappa_2^{15} + 191980286687434545\kappa_1^{12}\kappa_2^{16} + 373600162343077395\kappa_1^{11}\kappa_2^{17} \\
& + 26654117097834493\kappa_1^{10}\kappa_2^{18} + 94462186400242197\kappa_1^9\kappa_2^{19} - 112459641067919644\kappa_1^8\kappa_2^{20} \\
& - 58932688180872330\kappa_1^7\kappa_2^{21} - 30317166816236766\kappa_1^6\kappa_2^{22} - 10190296532147550\kappa_1^5\kappa_2^{23} \\
& - 1260751770087705\kappa_1^4\kappa_2^{24} - 183530830884975\kappa_1^3\kappa_2^{25} + 4003879094775\kappa_1^2\kappa_2^{26} \\
& - 164509592625\kappa_1\kappa_2^{27} + 69075483750\kappa_2^{28}. \tag{60}
\end{aligned}$$

C Parametrization of hypersurfaces using tesseral spherical harmonics

Let $\mathbb{S} := [0, 2\pi) \times [0, \pi]$ be the parameter domain of the unit sphere in \mathbb{R}^3 . Then, the tesseral spherical harmonics $\mathcal{Y}_l^m : \mathbb{S} \mapsto \mathbb{R}$ being defined as

$$\mathcal{Y}_l^m(\varphi, \theta) = \sqrt{\frac{2l+1}{4\pi} \frac{(l-|m|)!}{(l+|m|)!}} \begin{cases} \sqrt{2} P_l^{|m|}(\cos \theta) \sin |m| \varphi & m < 0 \\ P_l^m(\cos \theta) & m = 0 \\ \sqrt{2} P_l^m(\cos \theta) \cos m \varphi & m > 0 \end{cases} \quad (61)$$

with the associated LEGENDRE polynomials

$$P_l^m(x) = \frac{(-1)^m}{2^l l!} \sqrt{(1-x^2)^m} \frac{\partial^{l+m}}{\partial x^{l+m}} (x^2 - 1)^l, \quad (62)$$

form an orthonormal basis of the square-integrable functions $\mathcal{L}^2(\mathbb{S})$, where

$$\delta_{lk} \delta_{mn} = \frac{1}{4\pi} \int_0^{2\pi} \int_0^\pi \mathcal{Y}_l^m \mathcal{Y}_k^n \sin \theta d\theta d\varphi. \quad (63)$$

Within this paper, we consider a class of star-shaped hypersurfaces $\Sigma \subset \mathbb{R}^3$ with parametrization

$$\Sigma = \{R \mathbf{e}_r : (\varphi, \theta) \in \mathbb{S}\}, \quad (64)$$

where $R : \mathbb{S} \mapsto \mathbb{R}$ and $\mathbf{e}_r := [\cos \varphi \sin \theta, \sin \varphi \sin \theta, \cos \theta]^\top$ denote the radius and radial unit vector, respectively. Herein, the third power of the radius instead of the radius itself is expressed in terms of spherical harmonics, i.e.

$$R^3(\varphi, \theta) = \sum_{l=0}^L \sum_{m=-l}^l c_l^m \mathcal{Y}_l^m(\varphi, \theta). \quad (65)$$

By recursive application of the contraction rule for spherical harmonics it can be shown that the order of R is $L/3$. However, the computation of the enclosed volume is considerably simplified, namely

$$|\text{dom}(\Sigma)| = \frac{1}{3} \int_0^{2\pi} \int_0^\pi \sum_{l=0}^L \sum_{m=-l}^l c_l^m \mathcal{Y}_l^m(\varphi, \theta) \sin \theta d\theta d\varphi = \frac{1}{3} \int_0^{2\pi} \int_0^\pi c_0^0 \mathcal{Y}_0^0(\varphi, \theta) \sin \theta d\theta d\varphi = \frac{\sqrt{4\pi}}{3} c_0^0. \quad (66)$$

Since this class of parametrizations degenerates at the poles, i.e. for $\theta \in \{0, \pi\}$, in order to ensure that $\Sigma \in \mathcal{C}^0$ the derivative of the radius with respect to the azimuthal angle φ needs to vanish, i.e. $\partial_\varphi R = 0$ for $\theta \in \{0, \pi\}$. Then, the outer unit normal at the poles becomes

$$\mathbf{n}_\Sigma|_{\theta \in \{0, \pi\}} = \frac{R \mathbf{e}_r - \partial_\theta R \mathbf{e}_\theta}{\sqrt{R^2 + (\partial_\theta R)^2}}. \quad (67)$$

For eq. (67) to be respectively unique obviously one requires the polar derivate to vanish at the poles as well, i.e. $\partial_\theta R = 0$ for $\theta \in \{0, \pi\}$. While the tesseral spherical harmonics by definition fulfill $\partial_\varphi \mathcal{Y}_l^m|_{\theta \in \{0, \pi\}} = 0$, it holds that

$$\partial_\theta \mathcal{Y}_l^m|_{\theta \in \{0, \pi\}} = \begin{cases} 0 & |m| \neq 1 \\ -\frac{1}{2} \sqrt{\frac{l(l+1)(2l+1)}{4\pi}} \cos^l \theta & |m| = 1 \end{cases}. \quad (68)$$

Hence we exclude modes with $m = \pm 1$ from the radius expansion, cf. eq. (65). For vanishing derivatives with respect to polar and azimuthal angle, the WEINGARTEN map at the poles becomes

$$\mathbf{W} = \frac{1}{R^2 \sin^2 \theta} \begin{bmatrix} \sin \theta \partial_{\varphi\varphi} R - \sin^2 \theta R & \partial_{\varphi\theta} R \\ \sin^2 \theta \partial_{\varphi\theta} R & -\sin^2 \theta (R - \partial_{\theta\theta} R) \end{bmatrix}. \quad (69)$$

Since by definition it holds that $\partial_{\varphi\varphi} R = \partial_{\varphi\theta} R = \partial_{\theta\theta} R = 0$ for $\theta \in \{0, \pi\}$, the parametrization is sufficiently smooth at the poles with principal curvatures $\kappa_i|_{\theta \in \{0, \pi\}} = -1/R$ and $\mathbf{n}_\Sigma|_{\theta \in \{0, \pi\}} = \mathbf{e}_r$.